
International Journal of Computer Vision

DOI: 10.1007/s11263-006-9780-x

Image Registration of Sectioned Brains

OLIVER SCHMITT
Institute of Anatomy, University of Rostock, Gertrudenstr. 9, D-18055 Rostock, Germany
schmitt@med.uni-rostock.de

JAN MODERSITZKI, STEFAN HELDMANN AND STEFAN WIRTZ
Institute of Mathematics, University of Lübeck, Wallstraße 40, D-23560 Lübeck, Germany
modersitzki@math.uni-luebeck.de
heldmann@math.uni-luebeck.de
wirtz@math.uni-luebeck.de

BERND FISCHER
Institute of Mathematics, Medical University of Lübeck, Wallstraße 40, D-23560 Lübeck, Germany
fischer@math.uni-luebeck.de

Received December 1, 2004; Revised February 22, 2006; Accepted April 27, 2006

First online version published in September, 2006

Abstract. The physical (microtomy), optical (microscopy), and radiologic (tomography) sectioning of biological objects and their digitization lead to stacks of images. Due to the sectioning process and disturbances, movement of objects during imaging for example, adjacent images of the image stack are not optimally aligned to each other. Such mismatches have to be corrected automatically by suitable registration methods.

Here, a whole brain of a Sprague Dawley rat was serially sectioned and stained followed by digitizing the 20 μm thin histologic sections. We describe how to prepare the images for subsequent automatic intensity based registration. Different registration schemes are presented and their results compared to each other from an anatomical and mathematical perspective. In the first part we concentrate on rigid and affine linear methods and deal only with linear mismatches of the images. Digitized images of stained histologic sections often exhibit inhomogenities of the gray level distribution coming from staining and/or sectioning variations. Therefore, a method is developed that is robust with respect to inhomogenities and artifacts. Furthermore we combined this approach by minimizing a suitable distance measure for shear and rotation mismatches of foreground objects after applying the principal axes transform. As a consequence of our investigations, we must emphasize that the combination of a robust principal axes based registration in combination with optimizing translation, rotation and shearing errors gives rise to the best reconstruction results from the mathematical and anatomical view point.

Because the sectioning process introduces nonlinear deformations to the relative thin histologic sections as well, an elastic registration has to be applied to correct these deformations.

In the second part of the study a detailed description of the advances of an elastic registration after affine linear registration of the rat brain is given. We found quantitative evidence that affine linear registration is a suitable starting point for the alignment of histologic sections but elastic registration must be performed to improve significantly the registration result. A strategy is presented that enables to register elastically the affine linear preregistered rat brain

sections and the first one hundred images of serial histologic sections through both occipital lobes of a human brain (6112 images). Additionally, we will describe how a parallel implementation of the elastic registration was realized. Finally, the computed force fields have been applied here for the first time to the morphometrized data of cells determined automatically by an image analytic framework.

Keywords: neuroimaging, human and rat brain serial sections, affine registration, elastic registration, matching, alignment, warping, 3D-reconstruction

1. Introduction

The three dimensional-reconstruction (3D-reconstruction) of images derived from physical (microtomy, serial sawing of plastinated structures), optic (conventional confocal microscopy, laser scanning confocal microscopy), and diagnostic imaging (magnet resonance imaging (MRI), functional magnetic resonance tomography (fMRI), computer tomography (CT)) need to be spatially reconstructed for the prupose of visualizing the three dimensional extension of structures. Meanwhile, the 3D-reconstruction and volume visualization delivers important information for preoperative planing in neurosurgery (Desgeorges et al., 1997) and other disciplines (Lamadø et al., 2000).

Since the physical principles of microscopical optics have been elaborated (Abbe, 1873) it has become customary to slice thick specimens in order to reduce mass thickness and provide translucent objects, for microscopy. The first 3D-reconstruction using serial sectioning and modelling via a wax plate technique has been published by Born (1883) followed by an epochmaking 3D-reconstruction of the retina (Sjöstrand, 1958). A few years later Glaser and Glaser (1965) demonstrated a computer generated 3D-reconstruction from images derived from serial sectioning analyzed by a light microscope. Since these striking works many articles dealing with different kinds of 3D-reconstructions based on microscopical data (transmission electron microscope (Bron et al., 1990; Gremillet et al., 1991), lightmicroscopy of semithin-sections (Schmolke and Fleischhauer, 1984; Schmolke, 1996), lightmicroscopy of 5 to 50 μm thick sections have been published (Schormann and Zilles, 1998; Ourselin et al., 2001b).

A disadvantage of sectioning, staining and mounting the sections on the slides is a lack of spatially perfect matching when the sections are superimposed. Nevertheless, such undesirable mismatching of successive sections must be corrected. Correcting mismatches or sequential alignment is called *registration*. Presently, registration of serial sectioned specimens is performed with digitized objects in terms of images although analog material can be registered as well (Sjöstrand, 1958). Because serial sectioning is a widely used technique to gain an insight into the three dimensional structure of one object or to get an idea of the distribution of biological objects (cells, fibers, proteins) in 3D, many anatomists and biologists regard it as indispensable. The problem arises as to *how to register*. Since there exist different kinds of registration techniques (Brown, 1992; van den Elsen et al., 1993; Maintz and Viergever, 1981; Lester and Arridge, 1999; Modersitzki, 2004) for different registration problems, in particular for the alignment of images of serial sections, we will concentrate in the first part of this contribution on affine linear registration in difference to other—especially nonlinear—techniques (Broit, 1981; Horn and Schunck, 1981; Bajcsy and Kovačíč, 1989; Christensen, 1994; Viola and Wells, 1993, 1997; Bro-Nielsen and Gramkow, 1996; Thirion, 1998; Modersitzki et al., 1999; Schmitt and Eggers, 1999; Schmitt et al., 1999) which will be considered in detail in the second part.

Prior studies presenting 3D-reconstructions based on serial sectioning of biological material have one aspect in common: the alignment is done manually (Ware and LoPresti, 1975; Dierker, 1976; Macagno et al., 1976, 1979; Perkins and Green, 1982; Johnson and Capowski, 1983; Street and Mize, 1983; Aferzon et al., 1991; Baumann and Scharf, 1994), semiautomatically or with algorithms which have been fitted to a specific series of images. Manual alignment is extremely time consuming if matching of many images is necessary and a number of different image stacks have to be registered. However, doing the registration in a manual mode limits information available regarding the quality of the registration and mismatches.

As a means to perform the registration automatically, a robust registration technique with well defined requirements as to the biologic material and its resulting

images have been developed, optimized and implemented. In a first approach we concentrated on preprocessing the raw images and on affine linear registration using the well-known and well-established principal axes transformation (PAT) (Barnard and Thompson, 1980; Hibbard and Hawkins, 1988; Alpert et al., 1990; Zhao et al., 1993; Rusinek et al., 1993; Banerjee and Toga, 1994; Schormann and Zilles, 1997). The PAT is able to improve the alignment due to translational and rotational (rigid) mismatches between two adjacent images. However, it is unable to correct shear components (Schormann and Zilles, 1997) and may not lead to optimal registration. Shearing plays an important role in images of serially sectioned biological objects (Schormann et al., 1997). Thus, PAT may not be the best registration technique for a histologic serial sectioning.

The results of the different registration experiments done in this work are presented by 3D-reconstructions and isoplanar visualizations to compare different rigid and affine linear registration methods. Essential modifications (robust version of PAT, first order statistics for parameter estimation) of affine linear registration techniques for histologic serial sectioning of rat brains are described. These modifications proved to be important to obtain high quality and user independent matched image stacks for 3D-reconstructions, 3D-visualizations and further spatial analysis.

However, the improvements are insufficient because we aim to register locally to obtain approximately the same relations of gravity centers of cells as in the intact brain. The 3D-reconstruction of gravity centers has several reasons which are examplified shortly in the following.

Beside the connectivity, receptor, neurotransmitter and molecular layout of neurons their spatial distribution and consequently their interneuronal distances are fundamental for neuronal information processing (Young, 1992, 1996; van Essen, 1997). Suppose, that the same neuronal population of a human forebrain with the same molecular layout is distributed in a spatial random manner. In such a model only the axons are shortened or elongated, whereas the dendritic structures, distribution of synapses and connectivities are preserved. The mean distances in between neurons which constitute micro-, macro- (Schlaug et al., 1995; Mountcastle, 1997) or hypercolumns (Okajima, 1986; Kuljis and Rakic, 1990; Tanaka, 1991; Yeshurun and Schwartz, 1999) and local circuits or micro-circuits (White, 1989; Abeles, 1991) that can be considered as functional entities of neuronal ensembles or cell assemblies (Hebb, 1949; Braitenberg, 1978; Palm, 1982; Gerstein et al., 1989), would increase and therefore the duration of transmitting action potentials, too. Such a modification would effect the integration of synchronized action potentials and the neuronal information processing (Arbib, 1995).

In order to develop an elementary and *neurocausal* understanding of neuronal information processing we elaborated a method to represent these basic structural information of neuronal tissue, i.e. the exact spatial localization of all neurons of a human brain.

To determine the exact spatial location of single neurons in brains confocal laser scanning microscopy (CLSM) seems to be a promising method. However, the depth of optical sectioning is limited to approximately 400 μm (Pawley, 1995) and neurons have to be demarked by a fluorochrome whereby the way of diffusion is relative long. Scanning whole human brain sections by a confocal microscope is not possible at present because there exist no CLSM that can shift sections continues over an area of 120 mm $\times$ 120 mm. Also μMRI (micro magnetic resonance imaging) technology (Benveniste and Blackband, 2002) has not reached such a resolution that is necessary to detect nonlabeled (Hoehn et al., 2002) single neurons whereby layer (Silva and Koretsky, 2002) and column (Thompson et al., 2003) specific activation signals can be imaged by the BOLD-technique. Since there are no other methods available than light microscopy to detect single neurons and characterize them by immunohistochemistry, hybridization or other techniques in a non-sectioned human brain it is essential to minimize the *disintegration* of the brain. This implies to section systematic and serial the whole forebrain in defined exactly parallel spatial planes instead of the production of tissue blocks of certain cortical areas or subcortical structures. Furthermore, it is important to disintegrate minimally the tissue structure because we aimed to reconstruct the whole spatial information of all neurons. This can be done more reliable and easier for practical reasons by sectioning in parallel planes serially because the resulting sections need not to be registered in a three-dimensional puzzle. However, producing large sections cause other problems.

The main problem is that relative thin (20 μm) histologic sections (Fig. 14(b)) are necessary to detect neurons by means of videomicroscopy (Schmitt et al., 2005). The resulting area of the sectioning is relative large with respect to its thickness. Thus, deformation artifacts are introduced with a large probability by a

chain of physical effects within tissue processing. All these physical forces have one feature in common: they are nonlinear and thus affect different and singular parts of the foreground objects in an image of digitized sections. Furthermore, these deformations are accompanied by micro- and macro-cracks, wrinkling, and partial loss of tissue (Figs. 15(c), 17(a), (b)). Therefore, after super-positioning of consecutive histologic sections, those areas which fitted to each other before histologic processing (i.e., sectioning, stretching, mounting, staining) do not fit together anymore (Fig. 17(c)) and the gravity centers of neurons in adjacent sections are displaced, too. Because the exact spatial localizations of neurons are necessary in order to develop the proposed spatial structural model as described earlier, the deformation of *posthistologic* positions must be corrected.

This means, that a suitable correction method that should work automatically must be applied to the deformed contents of images. Because the imaged effects of physical deformations should be eliminated, it seems reasonable to use a physical model that can describe the behavior of elastic materials. The theory of elasticity delivers the theoretic framework that can be applied to images, too; (cf., e.g. Sokolnikoff, 1956; Green and Zerna, 1968; Green and Adkins, 1970; Budo, 1990; Lurie, 1990; Kosevich, 1995; Russo, 1996; Ciarlet, 2000; Fu and Ogden, 2001). Broit (1981) and Bajcsy and Kovačíč (1989) were the first authors who published this idea of applying elasticity theory to deformed image contents in order to correct the deformation to the non-deformed state. The roots of this idea are going back to works of Barnea and Silverman (1972), Fischer and Elschlager (1973) and Widrow (1973). Generally, such a concept of aligning an image to another is known as *image registration* (Brown, 1992; Maurer and Fitzpatrick, 1993; Toga and Banerjee, 1993; van den Elsen et al., 1993; Maintz and Viergever, 1981; Lester and Arridge, 1999; Hill et al., 2001). The elastic registration has been applied since 1981 by many authors (Christensen, 1994; Schormann and Zilles, 1998). Formulating the registration problem in a variational setting based on a distance measure and a regularizer, it is possible to solve it without further information on the underlying deformations or the underlying images, like, e.g., landmarks (Bookstein, 1984; Amit et al., 1991).

There exist only a few attempts to determine the material behavior of fresh brain tissue (Miller and Chinzei, 1997). However, no measurements of paraffin embedded tissue at different temperature and applications of forces like sectioning are available. In addition, it is questionable to improve the quality of the elastic model, since the deformation also stem from different forces, like, e.g., thermic processes.

The scope of this study aims to present the results of whole brain preparation, serial sectioning, large histologic section staining, digitalization and applying elastic registration to the images of deformed histologic sections. In this preliminary work we will present first results of an elastic registration of 100 sections from altogether 6112 sections through the occipital lobes of a human brain.

2. Material and Method

2.1. Material and Histologic Staining

An adult male Sprague-Dawley rat was anesthetized with an intraperitoneal injection of Nembutal and Rompun in 0.9% NaCl. The blood was washed out with 100 ml of Ringer-Heparin solution through the left ventricle by transcardial perfusion. The brain was then removed from the cranial cavity and fixed for 48 hours in a phosphate buffered 4% formaldehyde solution (pH 7.0) followed by rinsing in tap water. The brain was dehydrated through an increasing concentration of ethanol solutions. Ethanol was substituted by three changes of xylene. After passing this intermedium it was embedded in paraffin wax (Paraplast Plus, Sheerwood (8889–502005), 58–60°C melting point). Using a sliding microtome (Polycut, Reichert Jung) sections of 20 μm thickness were produced. To minimize the deformation introduced by the sectioning process, frontal sections from the olfactory bulb to the cerebellum were made. This lead to 503 tissue sections for this particular brain.

The slices are positioned manually on standardized gelatinized slides. The sections were stained in gallocyanin chromalum and mounted with Entellan (Merck 1.07961.0500). An extensive overview of various suitable stainings and their properties with respect to image analysis is given in Schmitt and Eggers (1997a,b).

The forebrain of a 65 years old human male without any neurologic or psychiatric disorders who died in consequence of a cardiac infarction was removed 11 hours postmortem. The brain was fixed in 4% phosphate buffered isotonic (0.9% NaCl) formalin solution for 3 months at 4°C. Before dehydration the brain had a volume of 1211 ml, a height of 108 mm (between the margo superior and margo inferior), a

width of 140 mm (between the frontal superior gyrus and supramarginal gyrus of both hemispheres) and a length (between the frontal pole and occipital pole) of 170 mm. After immersion fixation the brain was dehydrated and embedded in paraffin wax at 60°C. This was followed by dispension and slow evacuation until 15 mmHg was reached for about 3 hours until no gas bubbles emerges out of the sulci anymore. The paraffin wax block was trimmed carefully and fixed on a block holder of the sliding microtome (Polycut®, Reichert Jung) (Fig. 14(b)). Just before the paraffin wax block on the block holder was shifted against the knife (D-knife, cutting angle 0°) a color image (1352 × 1795 pixels, 24 Bit) depicted from the surface of the wax-block of the embedded brain was transmitted to a computer (Fig. 15(b)). Sectioning was followed by flattening the jolted sections in a 40°C warm water bath.

Small wrinkles and folds are removed by teasing apart, using forceps. After flattening a section it was manoeuvred very carefully on special manufactured slides. The section are blotted lightly with moistened blotting paper to remove excess water and to increase contact between section and slide. After drying the prepared sections for at least 24 hours at 37°C they can be de-paraffined via xylene in a descending series of 2-propanols. This is followed by staining in gallocyanin chrome alum (a histologic section is shown on the flat bed scanner in Fig. 14(c)) because the perikaryon staining that also reacts with RNA and DNA gives sufficient homogeneous results, i.e. no trends of the staining intensity within the section are visible (Schmitt and Eggers, 1997a,b). The latter effect is important for a reliable image analysis of the homogeneous stained neurons. After the staining sections were dehydrated in ascending ethylalcohol solutions and cleared in three xylene dealcoholizing agents. For the whole deparaffination, staining and dehydration procedure we have constructed a transport device of stainless steel which do not interact with the gallocyanin chrome alum staining and which is able to transport up to 50 large histologic sections. This is important because 6112 sections of the brain were produced and had to be stained. After dehydration the sections were embedded in Entellan (Merck, 1.07961) and mounted under a cover glass (Fig. 14(c)).

2.2. *Digitizing*

Each section of the rat brain was digitized using a high resolution transparent flat-bed scanner (FBS) at a resolution of 6 μm per pixel length, see Schmitt and Eggers (1999) for details. Finer structures like laminations, subcortical nuclei and nerve fiber tracts can already be observed at this resolution. The digitization results in $m_\nu \times n_\nu$ images S^ν, $\nu = 1, \ldots, N = 503$, where m_ν varies between 913 and 1275 and n_ν varies between 1280 and 1883. The images have gray values in [0, 255]. Thus, each section is now represented by a matrix $S^\nu \in [0, 255]^{m_\nu \times n_\nu}$, where $S^\nu_{i,j}$ represents the gray value at the pixel (i, j). For simplicity of presentation, we assume that the images are embedded into 1900×1900 frames with unique background (gray value: 255), such that $S^\nu \in [0, 255]^{1900\times 1900}$ for all ν. We present registration results for the 1900 × 1900 sequence as well as for a down-scaled 512 × 512 sequence.

Before embedding and staining, the human forebrain was tomographied by a Magnetom SP4000 (1.5 T, T_1 weighted, Siemens) in order to receive a series of images of the brain before shrinkage caused by the embedding procedure effect the brain. The section thickness was 1 mm, 122 images were produced, with a size of 512 × 512 pixels.

The stained sections of the human forebrain were digitized by a high resolution transparent flat bed scanner (FBS) (DuoScan, Agfa) (Fig. 14(c)) at a resolution of 800 ppcm, i.e., 12.5 μm per pixel edge length. This results in gray tone images $B^{(\nu)}$, where ν runs through all 6112 sections (Fig. 15(b)). Each image is an m-by-n matrix, $B^{(\nu)} = (b^{(\nu)}_{i,j})_{i=1\,j=1}^{m\;n}$, with gray-values $b^{(\nu)}_{i,j} \in \{0, \ldots, 255\}$, where m and n do depend on ν.

The images were compressed lossless by the Lempel-Ziv-Welch algorithm as tif-files and stored on CD-ROMS. The uncompressed data of all FBS images are approximately 283 GB large. The smallest image has a size of 5000 × 2000 pixels and the largest 11000 × 7000 pixels (Fig. 16). The sections were digitized all with the same orientation. Therefore, they were preregistered coarsely by the person who controlled the scanner. Furthermore, the mean intensity was adapted for those sections which were stained slightly more intense so that stronger inhomogeneities as a result of fluctuations of the section thickness or slight staining inhomogeneities were compensated.

2.3. *Hardware and Software*

The computations were performed on a Pentium III (1 × 1 GHz, 4 GB RAM, Linux) under MATLAB

(6.2). The final visualization was obtained using T3D (Fortner, 1999) and KS400 (Zeiss, 1992).

2.4. Preprocessing

Before the images are aligned, they must be preprocessed because the affine registration technique applied here is based on gray level intensities. Fluctuations of the gray value distributions due to variations in section thickness, staining and illumination inhomogeneities can be adapted by the evaluation of gray value distributions of the image foreground. The following preprocessing steps (Fig. 1) have been applied.

1. *Segmentation:* We normalize such that the image background is zero and foreground is greater than zero. This was performed by a segmentation based on a simple threshold (Fig. 2B). The threshold τ^ν is controlled by the mean μ^ν and variance σ^ν of the gray value distribution of each image,

$$\mu^\nu = \theta^{-1} \sum_{(i,j)\in\Theta} S^\nu_{i,j},$$
$$\sigma^\nu = \theta^{-1} \sum_{(i,j)\in\Theta} \left(S^\nu_{i,j} - \mu^\nu\right)^2,$$

where $\Theta = \{(i, j) : S^\nu_{i,j} \neq 0\}$, denotes the set of non background pixels and θ the number of its elements. The threshold is $\tau^\nu = \max\{0, \mu - 2\sigma\}$.

This approach delivers satisfying segmentation results after testing it with three different stacks of images of histologic brain sections.

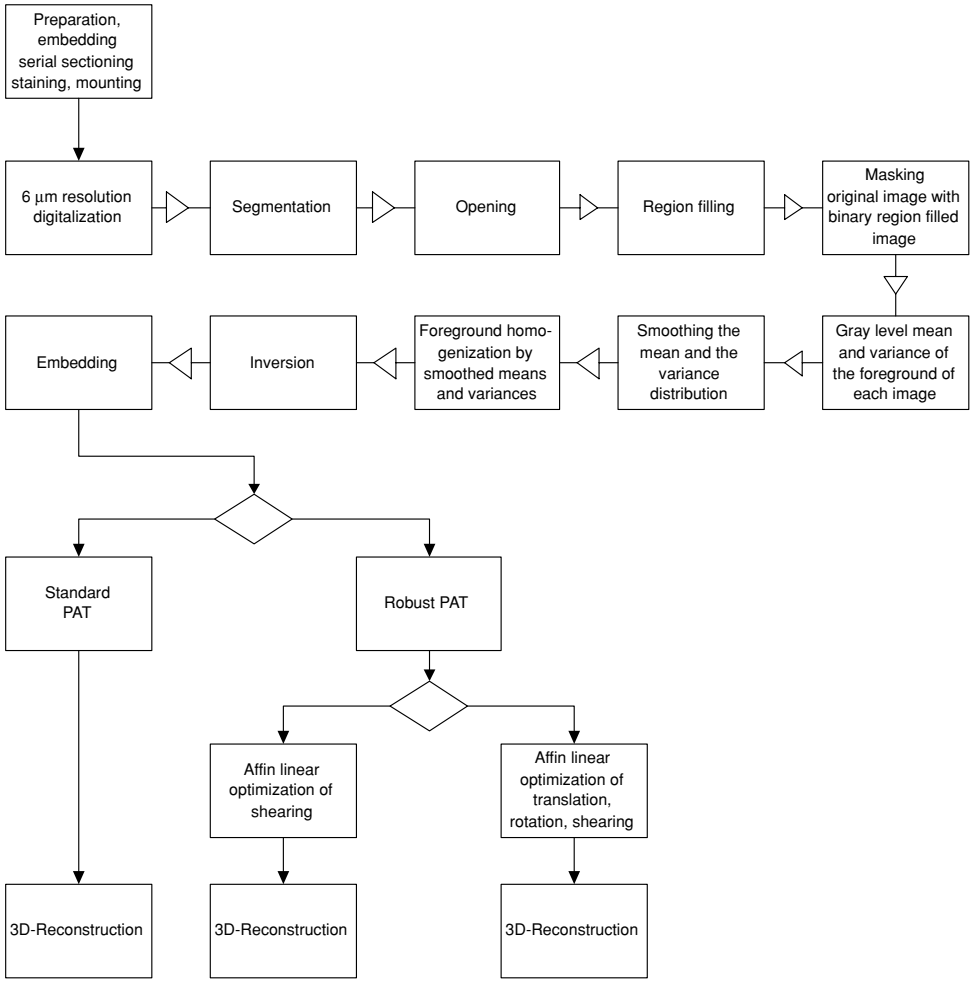

Figure 1. Flowchart of the preprocessing steps and registration schemes.

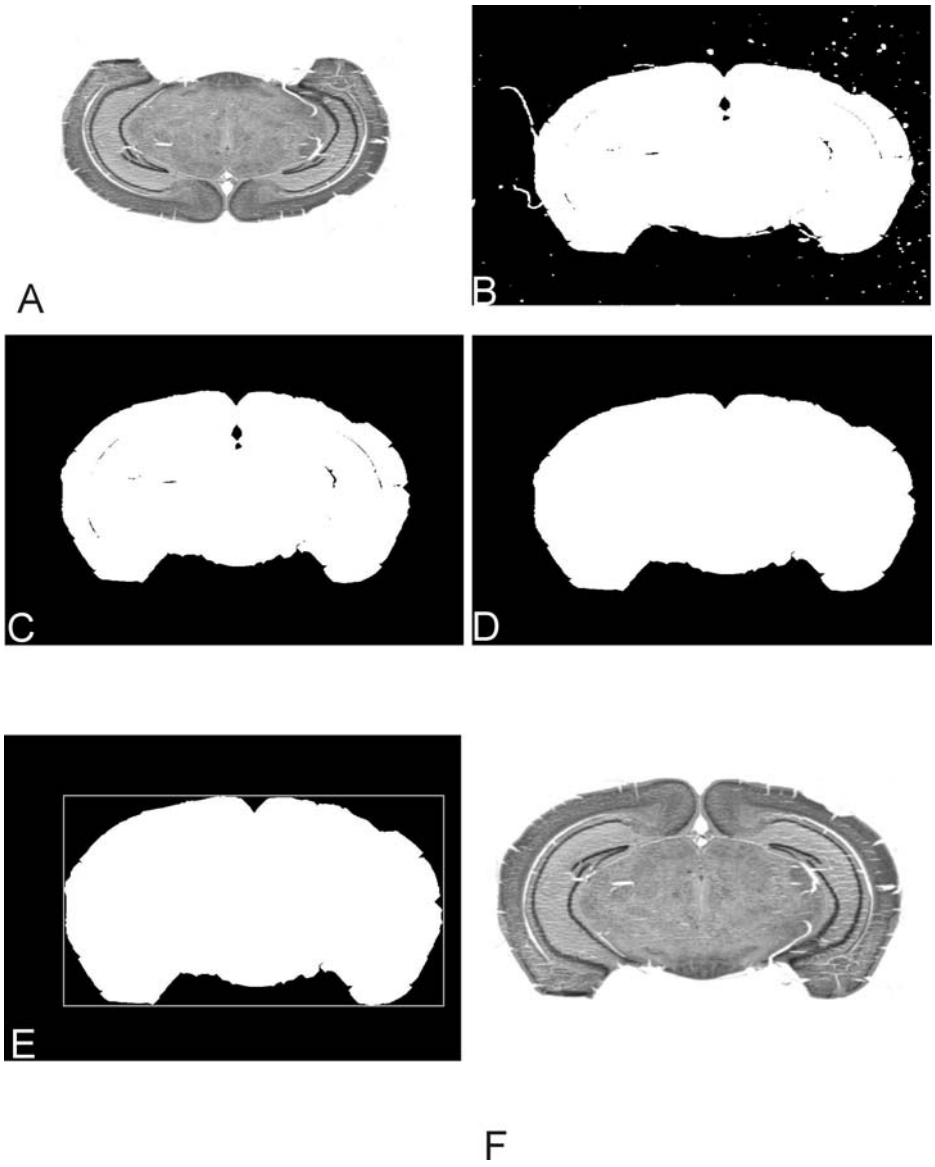

Figure 2. Image processing steps before registration. (A) The original image of a coronal section through a brain of a Sprague-Dawley rat. Due to projection within digitization, the image is mirrored around the x-axes. Before further processing steps, it is mirrored back. (B) Segmented binary image. (C) Image after binary opening. (D) Image after filling. (E) Determining the largest x-maximum and the largest y-maximum of the foreground objects over the whole image stack. (F) Each image is embedded into a background filled image of the size as given by the largest x maximum and y maximum that has been previously found.

2. *Morphologic operations:* Opening (Fig. 2(C)) and region-filling (Fig. 2(D)) were performed as described by Dougherty (1993).
3. *Masking:* The so far pre-processed binary image is used as a mask for the original image. In order to avoid dispensable notation, we denote the masked image again by S^ν. Only such pixels of the inverted gray level image were copied into the resulting image that coincide with the foreground pixels of the binary filled image.
4. *Inversion and Homogenization:* The images are inverted and normalized such that the background values become zero ($S^\nu_{i,j} \leftarrow \max_{i,j}\{S^\nu_{i,j}\} - S^\nu_{i,j}$). For each image we compute the mean gray-value μ^ν

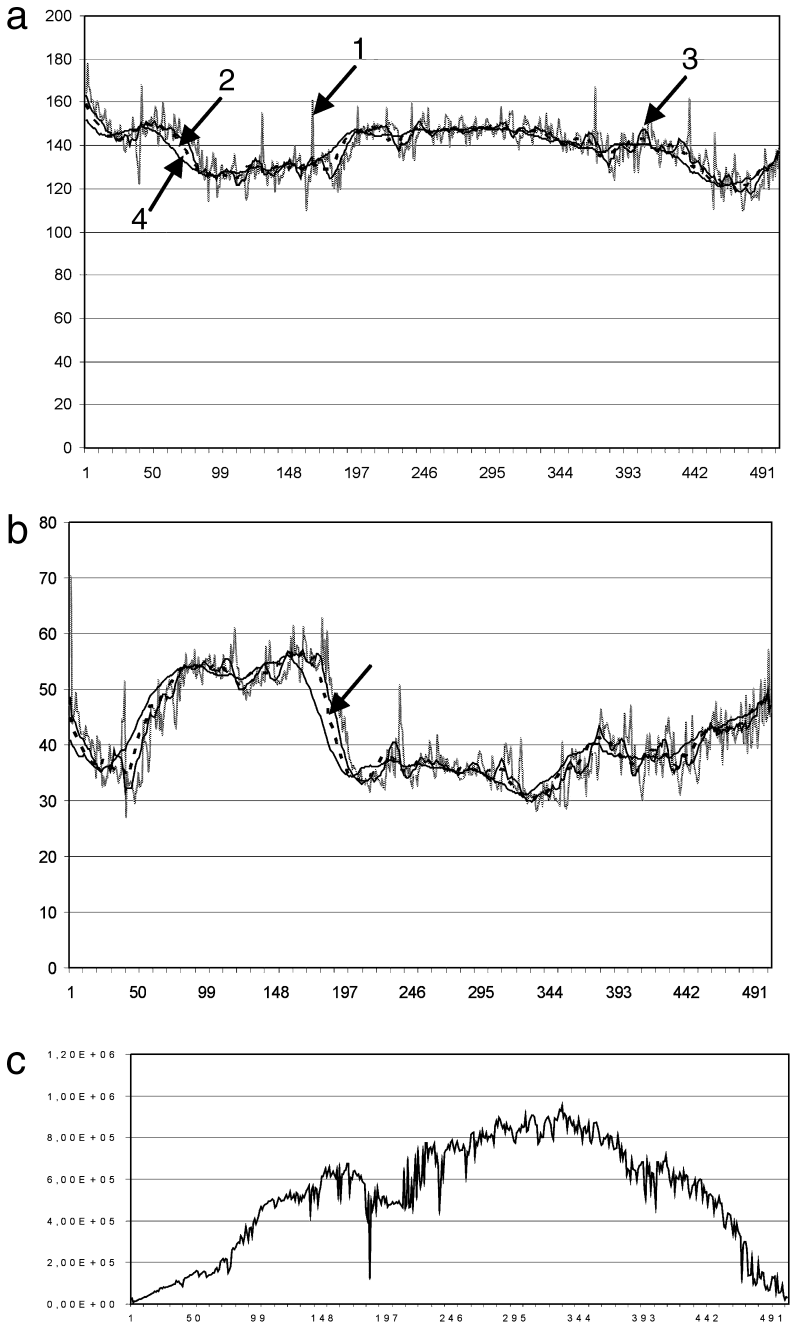

Figure 3. The foreground of each image is segmented and its mean and standard deviation of intensities calculated. The distribution of mean intensities over all 503 foregrounds in the images is shown in (a) by arrow 1. The distribution is smoothed with a sliding averaging window of the size of 8 (arrow 2), 16 (arrow 3) and 32 (arrow 4). In order to show that the size of the averaging window has only minor effects on the run of the curve different sizes of windows are presented. The standard deviations of the foregrounds of each image are summarized in (b). The arrow indicates the curve calculated by a sliding average of 8. In (c) the sum of pixels of each foreground object is plotted. The distribution coincides with the macroscopic body of the rat brain. It can be used to detect stronger differences of adjacent foregrounds that present loss of tissue or artifacts within the periphery of the object of interest.

(brightness) and the standard deviation σ^ν (contrast) on the set of non-zero pixels Θ,

$$\mu^\nu = \frac{1}{\theta} \sum_{(i,j)\in\Theta} S^\nu_{i,j},$$
$$(\sigma^\nu)^2 = \frac{1}{\theta} \sum_{(i,j)\in\Theta} \left(\mu^\nu - S^\nu_{i,j}\right)^2$$

Filtering the sequences μ^ν, σ^ν, $\nu = 1, \ldots, N$, by a sliding mean filter of length $2k+1$ (where we used $k = 7$ with success), we obtain smoothed parameters $\hat{\mu}^\nu$,

$$\hat{\mu}^\nu = \frac{1}{2k+1} \sum_{j=-k}^{k} \mu^{\nu+k}, \quad \hat{\sigma}^\nu = \frac{1}{2k+1} \sum_{j=-k}^{k} \sigma^{\nu+k},$$

where $\mu^\nu = \mu^1$ and $\sigma^\nu = \sigma^1$ for $\nu < 1$ and $\mu^\nu = \mu^N$ and $\sigma^\nu = \sigma^N$ for $\nu > N$, respectively. Note that $\hat{S}^\nu$ with

$$\hat{S}^\nu_{i,j} = \hat{\mu}^\nu + \frac{\hat{\sigma}^\nu}{\sigma^\nu}\left(S^\nu_{i,j} - \mu^\nu\right) \quad \text{for } (i,j) \in \Theta \quad (1)$$

has mean $\hat{\mu}^\nu$ and standard deviation $\hat{\sigma}^\nu$. However, the gray-values of $\hat{S}^\nu_{i,j}$ may no longer valid. Thus, we apply an obvious rounding of these numbers and obtain a homogeneous image stack (Fig. 3). Note that due to rounding, the parameters of the resulting image $\hat{S}^\nu$ may not exactly fit the defaults. A repetition of the computation improves the results.

This approach may propagade errors due to large differences in the gray level distribution. Since we have optimized the staining and sectioning protocols Schmitt and Eggers (1997a,b) such strong variations do not occur. There exist further sophisticated techniques (Dauguet et al., 2004; Malandain and Bardinet, 2003) that solve homogenization problems with large distribution difference very efficient.

5. *Embedding:* The homogenized images are embedded within the center of a new image. The width and height of this image is larger than the maximal diameter of the largest foreground object of the stack of images.

2.5. *Principal Axes Based Registration*

The backbone of our affine linear registration is a variant of the principal axes transformation (PAT). The PAT registration has been introduced to image processing by Hu (1962) (see also Hibbard et al., 1987; Alpert et al., 1990).

The idea is to find a restricted affine linear map $\phi : \mathbb{R}^2 \to \mathbb{R}$,

$$\phi(x) = Ax + b = \begin{pmatrix} a_1 & a_2 \\ a_3 & a_4 \end{pmatrix} \begin{pmatrix} x_1 \\ x_2 \end{pmatrix} + \begin{pmatrix} b_1 \\ b_2 \end{pmatrix},$$

such that a reference image and the mapped template image become similar.

PAT registration is strongly connected to the computation of moments. Moments are used in classical mechanics to characterize rigid bodies by the spatial distribution of their masses (Symon, 1971). In our application, the histologic sections are considered as mass distributions of rigid bodies. From this distribution we deduce geometrical features such as the mass centroid, the principal axes (Fig. 4) and the extension of the body with respect to the principal axes. The idea of PAT registration is to map the template image such that the geometrical features of the mapped template coincide with those of a reference image.

Though PAT registration is well understood, easy to compute, and fully automatic, it has some drawbacks. One of the main drawbacks is that PAT registration is not able to resolve shear components (Schormann and Zilles, 1997) of a deformation which definitely arise in our application.

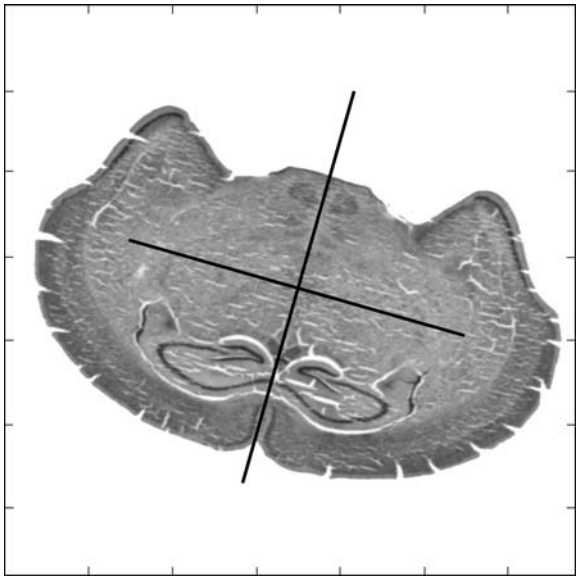

Figure 4. The principal axes of one image (no. 345) of the processed image stack is shown here.

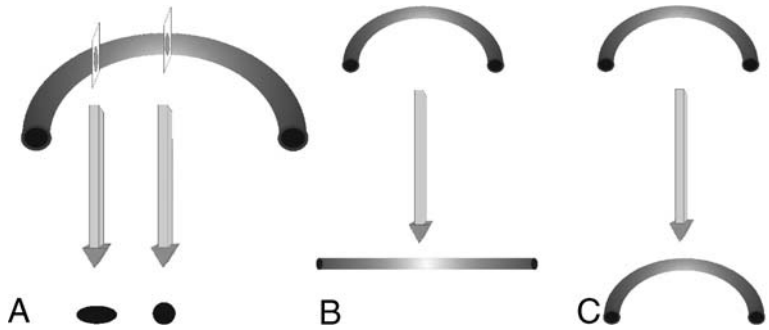

Figure 5. The rigid and\or affine linear registration methods may affect the spatial geometry of an object in dependence of the structure of data and the original shape. This sketch shows a curved 3D-object that is sectioned (A). We would expect a complete and unwanted destruction of the 3D-geometry of the biologic object (B) after aligning the sections from (A) only if the images of the sections are binary. Using gray tone images, the 3D-geometry is preserved within the affine linear registrations applied here. However, smaller misalignments can be avoided (C) only by bimodal registration using a 3D-data of undistorted reference images.

If the images to register would contain binary information only, the underlying sectioned body is curved and the projection or section planes are parallel then elliptic to round shaped objects may occur (Fig. 5) after registration and reconstruction. In this example each centroid of a foreground object in the binary images is calculated at the same image location and a curved tube would be transformed by the PAT method into a straight tube because the foreground is symmetric and foreground pixels have the same intensity or mass. Therefore, it is not possible to decide if a foreground such as a filled circle must be shifted or rotated in relation to foreground in the following image. If the pixel intensities are greater than 2 and not distributed symmetric such as those in gray value images of brains the original geometry will be *preserved more* but not totally because each pixel intensity contributes to the location of the centroid. This issue is analysed and disccused in great detail in Malandain et al. (2004). However, a total geometry preserving procedure must take into consideration a stack of reference images of the same object. Such a reference can be obtained by scanning the postmortem brain by MRI (Ourselin et al., 2001b; Schormann and Zilles, 1998; Schormann, 1996) before the histologic procedure will be performed.

Another drawback is that the results of PAT registration are not based on a distance measure between adjacent images and has thus no intensity based optimality criterion. Therefore, we combine the PAT approach with two minimizing techniques. In both optimization approaches the sum of squared differences (*SSD*) were minimized between the reference and an appropriately deformed template.

2.5.1. Standard Principal Axes. Our derivation for the standard PAT is slightly different than usual (Hibbard et al., 1987; Alpert et al., 1990; Schormann and Zilles, 1997). We view an image as a density function S, i.e. $S(x) \geq 0$ and $\int_{\mathbb{R}^2} S(x)dx = 1$. The last property can easily be fulfilled by re-scaling the gray values of the image. Choosing a set of reference densities G, we are looking for the best approximation $\hat{S} \in G$ of S with respect to the Kullback-Leibler distance (Kullback and Leibler, 1951),

$$\hat{S} := \arg\min \left\{ \int_{\mathbb{R}^2} S \log \frac{F}{S}\, dx : \ F \in G \right\}.$$

We then use geometrical properties of $\hat{S}$ in order to describe S. For example, if one chooses the set of Gaussian densities,

$$G := \{g_{A,b} : \mathbb{R}^2 \to \mathbb{R} \mid A \in \mathbb{R}^{2\times 2}, \det A > 0, b \in \mathbb{R}^2\},$$

where

$$g_{A,b}(x) := \frac{1}{2\pi\sqrt{\det A}} \exp\left(-\tfrac{1}{2}(x-b)^{\mathrm{T}} A (x-b)\right),$$

the solution is given by $A = \mathrm{Cov}_S$ and $b = c_S$. Here, c_S denotes the center of mass and Cov_S the covariance matrix of the density S. Using moments

$$m_{i,j} := \int_{\mathbb{R}^2} x_1^i x_2^j S(x_1, x_2) d(x_1, x_2)$$

we have

$$c_S = (m_{1,0}, m_{0,1})^{\mathrm{T}}, \quad \mathrm{Cov}_S = \begin{pmatrix} m_{2,0} & m_{1,1} \\ m_{1,1} & m_{0,2} \end{pmatrix} - c_S c_S^{\mathrm{T}}.$$

Since Cov_S is symmetrically positive semi-definite, it permits an eigenvalue decomposition (Golub and van Loan, 1989)

$$\mathrm{Cov}_S = D(\rho^S)\Sigma^S D(-\rho^S) \tag{2}$$

where $D(\rho)$ denotes a rotation matrix and Σ is a scaling matrix,

$$D(\rho) := \begin{pmatrix} \cos\rho & -\sin\rho \\ \sin\rho & \cos\rho \end{pmatrix}, \quad \Sigma := \begin{pmatrix} \sigma_1^2 & 0 \\ 0 & \sigma_2^2 \end{pmatrix}.$$

The geometrical features to be used are the center of gravity $c_S = (c_1^S, c_2^S)^{\mathrm{T}}$, the principal axes spanned by $(\cos\rho^S, \sin\rho^S)^{\mathrm{T}}$ and $(-\sin\rho^S, \cos\rho^S)^{\mathrm{T}}$, and the standard deviation of the distribution with respect to the principal axes, σ_1^S and σ_2^S, respectively. The five parameters

$$\left(c_1^S, c_2^S, \rho^S, \sigma_1^S, \sigma_2^S\right) \tag{3}$$

can easily be determined from the moments $m_{i,j}$, where $(i, j) = (0, 1), (1, 0), (2, 0), (1, 1)$, and $(0, 2)$.

2.5.2. Robust Principal Axes. However, as it is well-known (Kent and Tyler, 1988), Gaussian density estimation is sensitive to outliers in the distribution and corrupted images due to such outliers occur frequently in images derived from thin histologic sections. Typical outliers are, for example wrinkles, disruptions, pieces of tissue that were torn out and artifacts. Thus, one may replace the set of Gaussians by the set of Cauchy densities,

$$C := \{c_{A,b} : \mathbb{R}^2 \to \mathbb{R} \mid A \in \mathbb{R}^{2\times 2}, \det A > 0, b \in \mathbb{R}^2\},$$

where

$$c_{A,b}(x) := C(1 + (x - b)^{\mathrm{T}} A(x - b))^{-3/2}$$

and the constant c has to be chosen such that $\int_\Omega c_{A,b}(x)dx = 1$. For computational issues, we refer to Kent and Tyler (1988).

Cauchy density estimation leads to a more robust representation of the initial image. The influence of mass far from the image centroid becomes dampened and thus the impact of outliers is reduced. For this reason, the robust approach is used throughout this paper (Fig. 6).

This phenomenon is demonstrated by comparing the geometrical features of the section S^{241} with those of the artificially perturbed section, cf. Table 1 and Fig. 6. As it is apparent from the figure and the numbers given in the table, the robust approach is clearly preferable.

2.6. Optimality Based Affine Linear Registration

The geometrical feature σ_1^v and σ_2^v of the homogenized images are used in order to estimate the spatial extensions of the objects displayed. In particular we used a

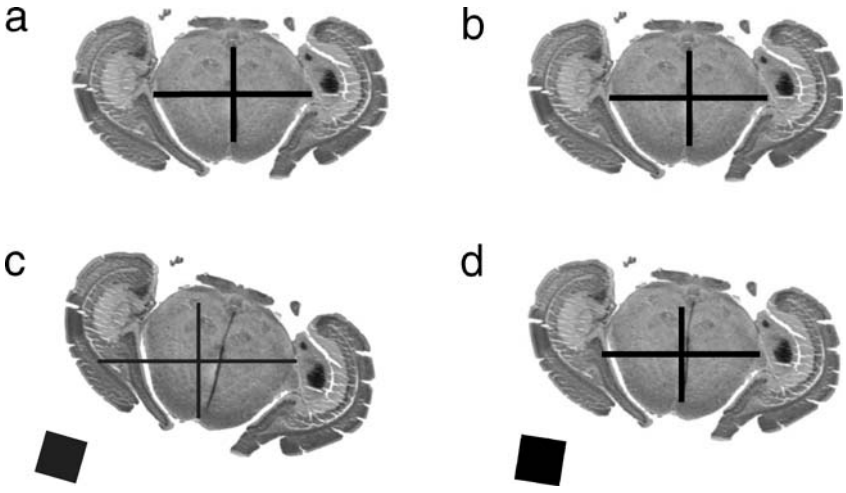

Figure 6. Results of a standard PAT and robust PAT of images with a quadratic artifact with a large mass. (a) Unperturbed image registered by the standard PAT. (b) Unperturbed image registered by the robust PAT. (c) Perturbed image registered by the standard PAT. (d) Perturbed image registered by the robust approach. Note, in (d) that the misregistration after robust PAT application is not as large as applying standard PAT in (c).

Table 1. Characteristics of the arbitrarily chosen image S^{241} (512×512 pixel) and an artificially perturbed copy using standard and robust characteristics, see also Fig. 6.

	Original		Perturbed	
	Standard	Robust	Standard	Robust
m	$6.0 \cdot 10^5$	$2.0 \cdot 10^6$	$6.6 \cdot 10^6$	$2.2 \cdot 10^6$
c_1	165.64	167.58	181.07	173.90
c_2	272.86	273.39	258.64	267.59
s_1	46.31	38.20	60.09	44.01
s_2	96.21	80.17	104.17	81.59
ρ	−0.0146	-0.0118	0.2860	0.1363

sliding median filter of length 15 for our estimation. Note, it is impossible to recover these extensions from an individual image. If one does not pay attention to this issue, one may map a sliced ball into a cylinder. For this reason, we do not use a full optimization with respect to all six parameters of a affine linear transformation.

Our optimization approaches (Fig. 1) are based on the minimization of the sum of squared differences (*SSD*)

$$\mathrm{SSD}[R, T; A, b] := \sum_x (T(Ax + b) - R(x))^2, \quad (4)$$

with respect to the matrix A and the transformation b. In the next subsections we discuss particular choices for A.

For the evaluation of $T(Ax + b)$ (T: template image, R: reference image) we exploit a bi-linear interpolation scheme and Euler coordinates. Since we are considering intramodal registration this cost function can be applied as proposed by different authors (Schormann and Zilles, 1998; Hajnal et al., 1995). Other promising similarity measures like mutual information (Holden et al., 2000) and gradient difference (Penney et al., 1998) were not investigated here.

In histological sectioning, shearing is a very likely deformation, because the sectioning is always performed from one fixed direction. Therefore, our first approach (α-*optimal*), is to optimize with respect to the shear.

In the second so-called *partial-optimal* approach, we optimize with respect to rotation, shearing and translation. In contrast to a full affine linear approach, the scaling of the transformation is not optimized but estimated from global parameters of the complete histological series. For both approaches the PAT registered images serve as starting points for a Gauss-Newton type optimization method.

2.6.1. Shearing Optimization (α-Optimal Approach). The optimization of the *SSD* with respect to the shear component of the deformation starts after robust PAT registration is passed.

The affine linear map $A_\alpha x + b_\alpha$ between two consecutive sections, the first one refereed to as a reference (R) and the second one as a template (T), is computed by minimizing the *SSD* (4) with respect to $\alpha \in \mathbb{R}$ setting

$$A_\alpha = D(-\rho^T)(\Sigma^T)^{\frac{1}{2}}\, D(\alpha)\, (\Sigma^R)^{-\frac{1}{2}} D(\rho^R)$$
$$\text{and} \quad b_\alpha = c^T - A_\alpha c^R,$$

and $\phi_\alpha(x_1, x_2)^T := A_\alpha(x_1, x_2)^T + b_\alpha$ where c_1^R, c_2^R, ρ^R and c_1^T, c_2^T, ρ^T are given by Eq. (3) for the reference and template image, respectively. The basic idea is to implicitly transform reference and template images into a normalized setting and than to optimize with respect to shear. Note that the formula integrated all three steps. $T \circ \phi_\alpha$ has the same center of gravity and principal axes as R. The parameter α is chosen, in order to minimize the distance between the images.

2.6.2. Partial Optimization (Partial-Optimal Approach). The α-*optimal* approach might be too restrictive. Thus, one may also allow optimize with respect to translation, rotation, and shearing, so-called *partial-optimal*. Making use of a singular value decomposition of a matrix A in (4) we have

$$A = A_{\beta,\gamma} = D(\beta) \begin{pmatrix} s_1 & 0 \\ 0 & s_2 \end{pmatrix} D(\gamma)$$

where s_1 and s_2 are obtained from the external estimates. The eigenvalue decomposition of the covariance matrix Cov_S (2) of an image S yields the rotation matrix $D(\rho)$ and the scaling matrix Σ, a diagonal matrix that contains the scalars s_1 and s_2. In our *partial-optimal* approach we use these original scalings of a section and only optimize with respect to the remaining four parameters of an affine linear transformation (here: β, γ, b_1, b_2). Thus we optimize the *SSD* in (4) w.r.t. the rotation angles β, γ and the translation b_1, b_2 but use fixed values of s_1 and s_2. Therefore, the affine linear map reads

$$\phi_{\beta,\gamma,b}(x) = A_{\beta,\gamma}\, x + b.$$

2.7. *The Overall Affine Linear Registration*

For the final registration of the image stack, the data-based breakpoint $\nu_0 := 241$ is chosen (image with the maximum number of non zero pixels). Let $R^{\nu_0} = S^{\nu_0}$ and $R^\nu = S^\nu(A^\nu x + b^\nu)$ otherwise, where (A^ν, b^ν) are computed from either the α-optimal, or the *partial-optimal* approach,

$$(A^{\nu\pm1}, b^{\nu\pm1}) = \arg\min\{\mathrm{SSD}[S^\nu, S^{\nu\pm1}; A, b] \mid A, b\}$$

and we take the "+" sign for $\nu < \nu_0$ and the "−" sign for $\nu > \nu_0$. Thus, 502 optimization problems for the rat brain sample are solved. The computations were performed on a Pentium III processor (1 GHz) equipped with 4 GB RAM under Linux. The computation time of 502 1024×1024 large images preprocessed as described was 13.95 minutes for standard and 84.87 minutes for robust PAT. The shearing optimization lasted 49.8 minutes and optimization of all three parameters takes 139.43 minutes after robust PAT was finished.

2.8. *Elastic Registration*

As described in the introduction histologic sections are effected by local nonlinear deformations which need to be reduced by the nonlinear approach *elastic registration*. The rheologic equation of state concatenates forces of tensions and distortions or extensions that can be determined experimentally. In most elastic models the embedded brain is assumed to behave at each point in the same manner with respect to deformations. Therefore, it is *homogeneous* with respect to material features. The brain was sectioned within a fixed direction, in this case from the superior to the inferior margin in the frontal plane. Because the outer border, i.e. cerebral cortex, consists of slightly other biological material than the white matter and the ventricles, we assume that material has more or less anisotropic features, i.e. the deformation effects of forces to the brain are depended from their direction.

In the case of the rat brain and the human forebrain that are soaked with paraffin wax we assume a homogeneous and isotropic state within sectioning. An inhomogeneous and anisotropic state within stretching the section in the warm water bath and the staining procedure should be kept in mind. Because we do not know the features of the embedded material, which is not a limiting factor for developing a generalizable and nonparametric nonlinear registration approach, we assume a linear relation between strain-tensor and stress-tensor. Let $u(x) = (u_1(x), u_2(x))^{\mathrm{T}}$ denote the displacement of a tissue particle located at a position $x = (x_1, x_2)^{\mathrm{T}} \in \mathbb{R}^2$. The Cauchy-St. Venont strain-tensor is denoted by V and the stress-tensor by Σ,

$$V := \begin{pmatrix} \epsilon_{1,1} & \epsilon_{1,2} \\ \epsilon_{2,1} & \epsilon_{2,2} \end{pmatrix} := \frac{1}{2}(\nabla u + \nabla u^{\mathrm{T}}),$$
$$\Sigma := \begin{pmatrix} \sigma_{1,1} & \sigma_{1,2} \\ \sigma_{2,1} & \sigma_{2,2} \end{pmatrix}. \tag{5}$$

Exploiting the homogeneity of the tissue sections, the strain- and stress tensor are simultaneously diagonalizable and can be rewritten in terms of an eigenvector basis. Let the eigenvalues of V and Σ be denoted by ϵ_j and σ_j, $j = I, II$, respectively. Moreover, under the homogeneity assumption, a linear model becomes

$$\begin{pmatrix} \epsilon_I \\ \epsilon_{II} \end{pmatrix} = \begin{pmatrix} E & -\upsilon E \\ -\upsilon E & E \end{pmatrix} \begin{pmatrix} \sigma_I \\ \sigma_{II} \end{pmatrix} \tag{6}$$

with some parameters $E, \upsilon \geq 0$, which are known as Young's elasticity module and Poissons's contraction ration. Introducing the so-called *Lamé-constants*

$$\mu := \frac{E}{2(1+\upsilon)} \quad \text{and} \quad \lambda := \frac{E\upsilon}{(1+\upsilon)(1-\upsilon)}, \tag{7}$$

Eq. (6) can be rewritten in general coordinates,

$$\sigma_{j,k} = 2\mu\epsilon_{j,k} + \lambda\,\mathrm{trace}(V)\,\delta_{j,k}$$
$$= \mu(\partial_{x_j} u_k + \partial_{x_k} u_j) + \lambda\,\mathrm{div}\,u\,\delta_{j,k}, \quad j,k = 1,2,$$

where $\delta_{j,k} = 1$, if $j = k$, and 0 otherwise. These equations describe the inner forces in a linear model of an elastic body. Let f denote an outer *force-field*. From Eq. (8) the equilibrium equation $f_j = \mathrm{div}\,\Sigma_j := \partial_{x_1}\sigma_{j,1} + \partial_{x_2}\sigma_{j,2}$, $j = 1,2$ which balances inner and outer forces, we obtain the Navier-Lamé-equations

$$\boxed{\begin{aligned} \mu\Delta u_1 + (\lambda+\mu)\partial_{x_1}\mathrm{div}\,u &= f_1, \\ \mu\Delta u_2 + (\lambda+\mu)\partial_{x_2}\mathrm{div}\,u &= f_2. \end{aligned}}$$

A more general approach to image registration is based on the minimization of the joint functional

$$\mathcal{J}[u] = \mathcal{D}[R, T; u] + \alpha\mathcal{S}[u], \tag{8}$$

where $R, T : \mathbb{R}^2 \to \mathbb{R}$ denotes the two images to be registered, $\mathcal{D}$ denotes an appropriate distance measure,

e.g., the so-called *sum of squared differences*

$$\mathcal{D}[R, T; u] = \frac{1}{2}\int_{\mathbb{R}^2} (T(x - u(x)) - R(x))^2\, dx, \quad (9)$$

and $\mathcal{S}$ denotes a regularizer, e.g., the elastic potential

$$\mathcal{S}[u] = \frac{1}{2}\int_{\mathbb{R}^2} \lambda\big(\partial_{x_1}u_1 + \partial_{x_2}u_2\big)^2 + \mu\big\{2\big(\partial_{x_1}u_1\big)^2 + 2\big(\partial_{x_2}u_2\big)^2 + \big(\partial_{x_2}u_1 + \partial_{x_1}u_2\big)^2\big\}\, dx,$$

and $\alpha > 0$ denotes a regularizing parameter (cf., Fischer and Modersitzki, 2002). The basic idea thus is to find a deformation of a template image (T) that simultaneously minimizes the difference between the deformed template and the reference image (R) and the deformation energy, respectively. This approach enforces similarity of the images as well as connectivity of the tissue. Note, in this notation $T(x - u(x))$ might be viewed as the non-deformed version of the template. Using the calculus of variation, a minimizer of (8) is characterized by

$$-f(u) + \mathcal{A}[u] = 0,$$

where

$$f(x, u(x)) = (T(x - u(x)) - R(x)) \cdot \nabla T(x - u(x)),$$
$$\mathcal{A}[u] = \alpha\mu\Delta u + \alpha(\lambda + \mu)\nabla \operatorname{div} u.$$

These are the Navier-Lamé equations with a particular force-field which stem from the Gâteaux-derivative of the distance measure (9).

An appropriate discretization of these equations finally leads to a fixed-point type equation for the unknown deformation field, cf. Eq. (10),

$$A\big(u_1^{(k+1)}, u_2^{(k+1)}\big)^{\mathrm{T}} = \big(f_1\big(u^{(k)}\big), f_2\big(u^{(k)}\big)\big)^{\mathrm{T}}. \quad (10)$$

2.9. Implementation

In principle, any method for solving a system of linear equations can be used to compute the solution of Eq. (10). However, a discretization of u_1 and u_2 with $m \times n$ points results in $N = 2mn$ unknowns (e.g. for 512×512 discretization points we end up with $N = 2^{19} = 524288$) and A becomes $N \times N$. For a standard LU-decomposition one needs to store $\mathcal{O}(N^2)$ real numbers and approximately $\mathcal{O}(N^3)$ floating point operations (see, e.g. Golub and van Loan, 1989). Thus, memory and computational requirements afford a particular treatment.

The implementation of our parallel algorithm for p processors can be divided into three parts (see Modersitzki et al., 1999) for a detailed description of the implementation on a 48 dual pentium cluster.

Let $\vec{X}_1$ and $\vec{X}_2$ refer to a spatial grid and $\vec{U}_j = u_j(\vec{X}_1, \vec{X}_2)^{\mathrm{T}}$ denote the values of the displacement field on the spatial grid. In an initialization step we set the iteration counter $k = 0$, $\vec{U}_1^{(k)} = \vec{U}_2^{(k)} = 0$. In the iteration, we compute the deformed template $T^{(k)}(x) := T(x - u^{(k)}(x))$ on the actual grid by using a bilinear interpolation scheme. Let $(x_1, x_2) \in [1, m] \times [1, n]$, $\xi_j := x_j - u_j(x_1, x_2)$, $d_j \in \mathbb{N}$, $j = 1, 2$, such that $d_j \le \xi_j < d_j + 1$. Then,

$$\begin{aligned} T^{(k)}(x_1, x_2) = {} & T(d_1, d_2)(d_1 + 1 - \xi_1)(d_2 + 1 - \xi_2) \\ & + T(d_1 + 1, d_2)(\xi_j - d_1)(d_2 + 1 - \xi_2) \\ & + T(d_1, d_2 + 1)(d_1 + 1 - \xi_1)(\xi_2 - d_2) \\ & + T(d_1 + 1, d_2 + 1)(\xi_1 - d_1)(\xi_2 - d_2). \end{aligned}$$

Using centered finite difference approximations for the derivatives, the actual force field on the spatial grid can be computed by

$$\begin{aligned} \vec{F}_1^{(k)}(x_1, x_2) = {} & \big(T^{(k)}(x_1, x_2) - R(x_1, x_2)\big) \\ & \cdot \frac{T^{(k)}(x_1 + 1, x_2) - T^{(k)}(x_1 - 1, x_2)}{2}, \\ \vec{F}_2^{(k)}(x_1, x_2) = {} & \big(T^{(k)}(x_1, x_2) - R(x_1, x_2)\big) \\ & \cdot \frac{T^{(k)}(x_1, x_2 + 1) - T^{(k)}(x_1, x_2 - 1)}{2}, \end{aligned}$$

where $T^{(k)}(x) = 0$ if $(x_1 - u_1^{(k)}(x),\ x_2 - u_2^{(k)}(x) \ni [1, m] \times [1, n])$ is not a grid point.

The linear system (10) is solved and computation is terminated if one of the three following conditions holds

$$\|u\| \ll 1, \quad \|f^{(k)}\| \ll 1, \quad \|R - T^{(k)}\| \ll \|R - T\|.$$

If we want to preserve and visualize histologic details like the lamination pattern of the cerebral cortex images of a minimal size of 512×512 pixels must be registered. Therefore, Fischer and Modersitzki (1999, 2001) have developed a fast solver based on the inverse Fast Fourier Transform that was also implemented in parallel on a high performance cluster (Böhme et al., 2002).

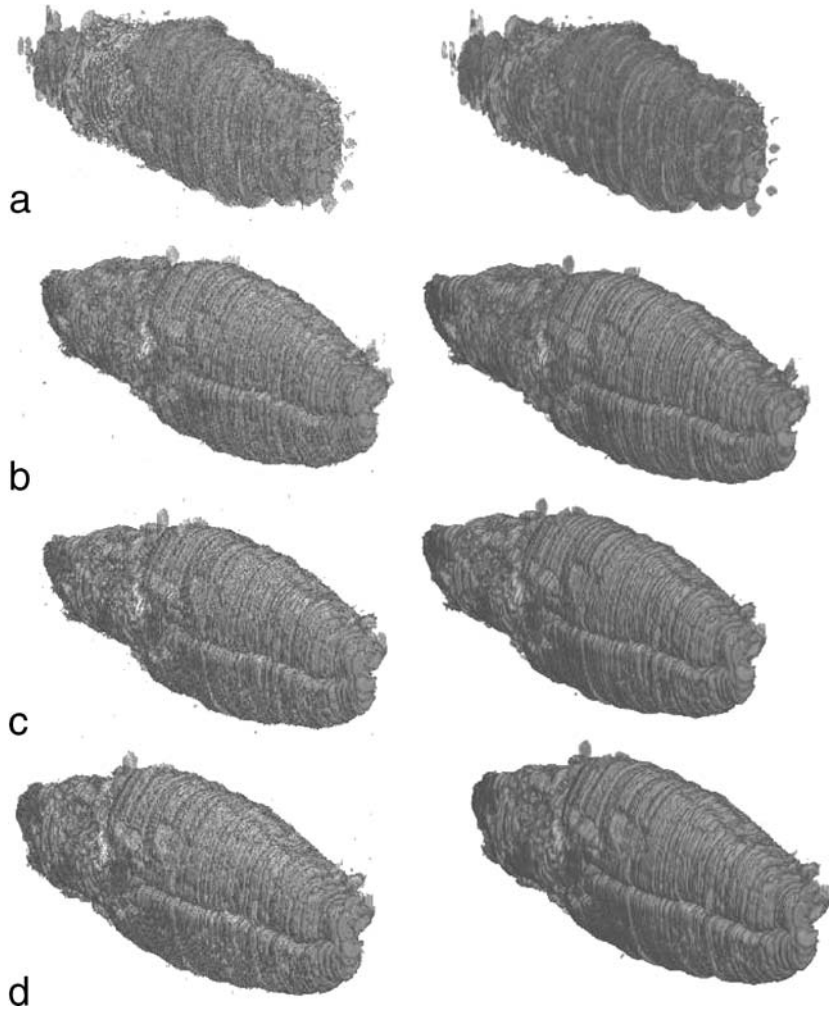

Figure 7. Overview of the 3D-reconstructions of (a) the original non-registered image stack (b) of the robust principal axes transformation, (c) of the shearing optimization and (d) optimization of translation, rotation and shearing. On the left side 3D-reconstructions without linear smoothing and on the right linear smoothed 3D-reconstructions are shown.

3. Results

3.1. Affine Linear Registration of the Rat Brain

In Fig. 7, the 2D-projections of 3D-reconstructed rat brain images are presented. The reconstructions are plotted in a smoothed and a non-smoothed version, respectively. All reconstructions depict the same view point of the brain. The non-registered image stack shows a blurred surface. The typical ellipsoid form of the 3D-body of the rat brain looks like a tube. At the rostral region small pieces of tissue lie somewhere in front of the telencephalon. These pieces of tissue belong to the olfactory bulb resp. accessory olfactory bulb. The cerebellum can be guessed by the posterior third in the reconstruction because there the surface seems to be more rough.

After applying exclusive PAT registration, the correct proportionated 3D-body of the rat brain, its surface, and macroscopic visible details like the longitudinal cerebral fissure, the cerebral hemispheres and the cerebellum with its lobes and lobules are identifiable. The small tissue sections of the olfactory bulb are aligned to their correct locations by the PAT.

The same results as described visually with respect to the 3D-reconstructions were found quantitatively, too. The robust PAT method leads in both examples of original and perturbed images to lower

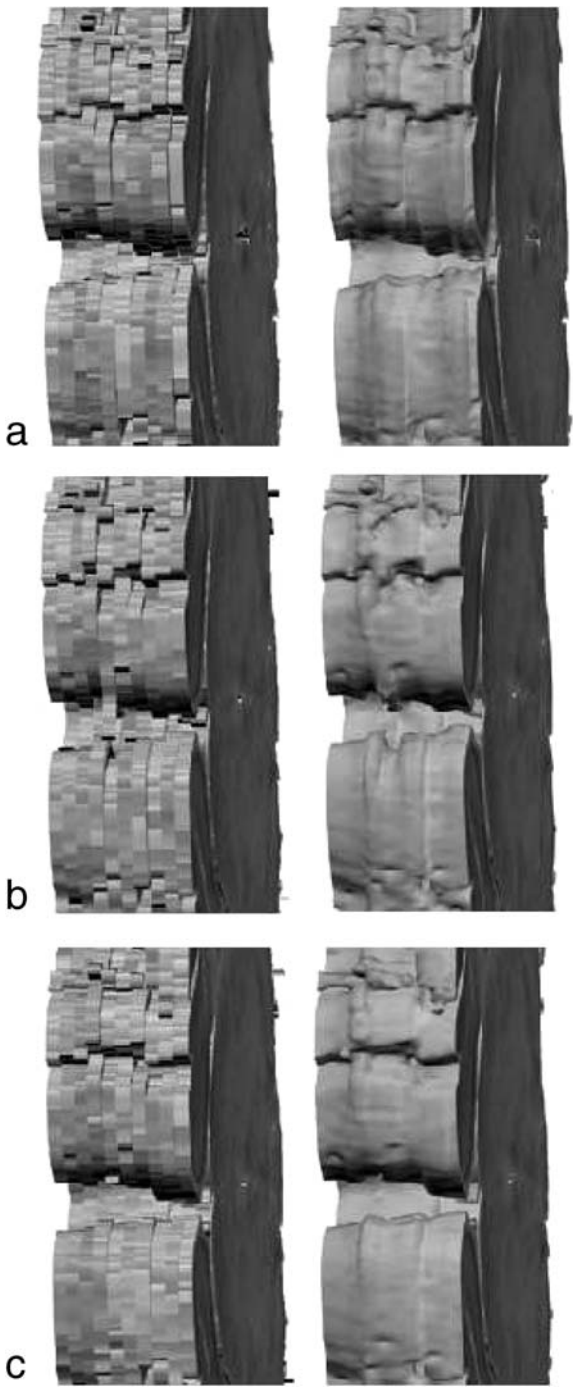

Figure 8. A region of interest within the longitudinal fissure of the rat brain (Fig. 7) is shown here in order to demonstrate details of the alignment. (a) PAT registration; (b) PAT registration plus shearing optimization; (c) PAT registration plus translation, rotation and shearing optimization. The surface of the 3D-reconstruction in (c) is slightly smoother. This means that the optimization of three parameters leads to a better result.

differences and therefore to a better registration result (Table 1).

Optimizing the translation after applying the robust PAT registration leads to a minor refinement of the surface of the brain reconstruction. The fact that a minor refinement is reached after the *α-optimal* approach can be seen more clearly after reconstructing a region of interest (ROI) around the longitudinal cerebral fissure (Fig. 8). The margin of the fissure is at some locations smoother than at the exclusive PAT registrations indicating that the adjacent images are better aligned.

The best quality of affine linear registration is delivered by the *partial-optimal* approach. Translation, shearing and rotation features are optimized after applying the robust PAT. The result is obviously better resp., the surface of the 3D reconstructed rat brain is smoother than in the *α-optimal* approach. This can be seen quite clearly in the 3D-reconstruction of the ROI as shown in Fig. 8(c).

Additionally, the mean *SSD*s of all methods for a sample of 21 adjacent images (330–350) of an embedded size of 1024 × 1024 pixels were calculated. The non-registered stack has a mean *SSD* of 36171. Robust PAT leads to a decrease of 47% and the standard PAT to 49% of the *SSD*. If shearing is optimized after robust PAT (55%, $\bar{x} = 16236.84$) or standard PAT (55%, $\bar{x} = 16239.95$) has been applied a further decrease was observed. The *SSD* of the robust PAT after rotation and translation optimization is 52%. Therefore, the shearing component contributes more to the deformation than rotation and translation within the affine linear registration step. The smallest *SSD* (59%) was calculated for the *robust partial-optimal* approach where translation, rotation and shearing have been optimized.

Different registration techniques lead in general to completely different reconstructions. Thus, there is in principal, no one-to-one correspondence between horizontal and sagittal sections of the 3D-reconstructions of the three different registrations. These visual impressions as described above can be recognized in isoplanar projections of the 3D-reconstructions, too (Fig. 9). Naturally, such virtual sections are only reasonable *after* registration and reconstruction. Therefore, the image processing chain has to be considered as an adequate constrain with resp. to the visualization of finer morphologic structures at high resolutions in these isoplanar sections. Such a fine structure can be seen in the horizontal isoplane in the brainstem (Fig. 10: e.g. abducence nucleus, trigeminal nucleus). The hippocampus formation and even the molecular layer of the cerebellar

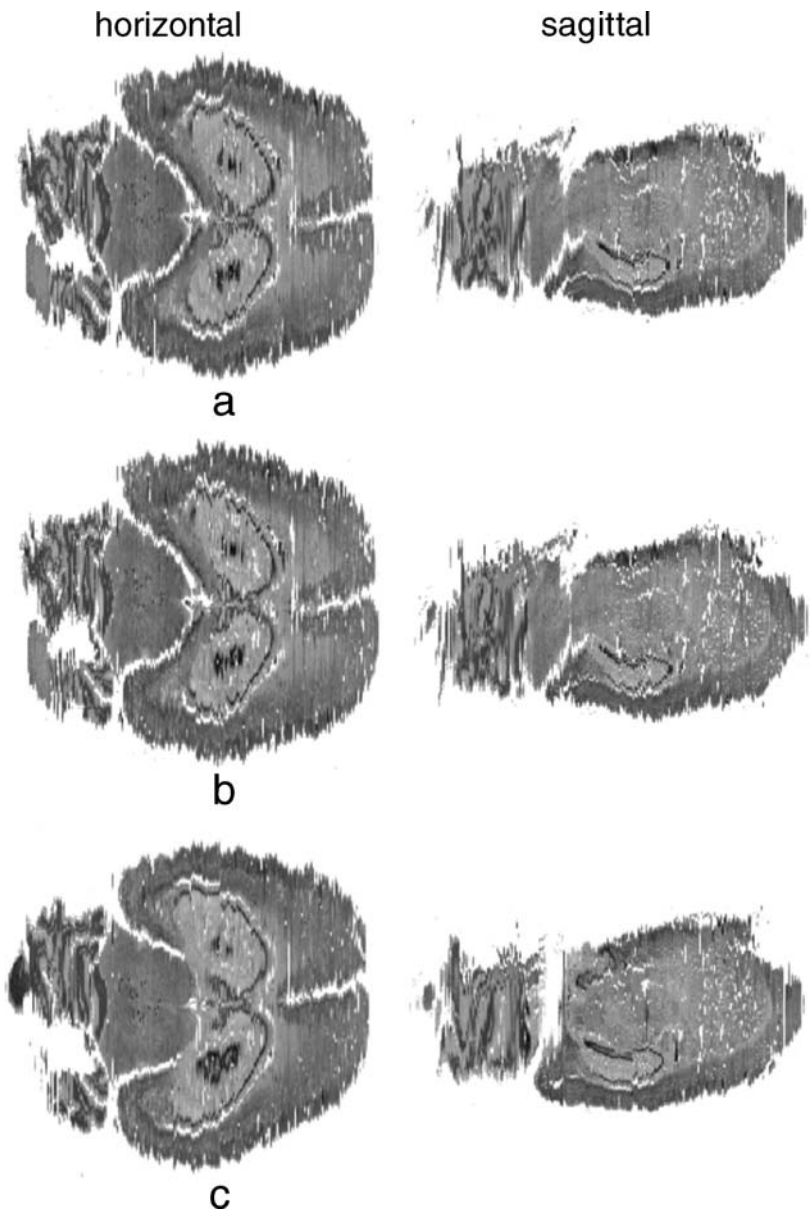

Figure 9. Isoplanar sections through 3D-reconstructions of three different registrations are presented here in the horizontal (left) and sagittal plane (right) for (a) PAT registration; (b) PAT registration plus shearing optimization; (c) PAT registration plus translation, rotation and shearing optimization.

cortex can be seen clearly. The white matter boarder of the cerebral cortex and the boarder of the molecular layer to the layer of the cerebellum can be differentiated as well. As mentioned before, it must be clear that the isoplanar sections of the exclusive PAT, α*-optimal* and *partial-optimal* approaches cannot be compared directly with respect to certain details because the optimization of shearing alone or shearing in combination with translation and rotation effect the 3D-geometry of the brain and consequently the *positioning* of small structures (Fig. 9). However, to make our results comparable, the most similar sections w.r.t. anatomic features were selected (original data: horizontal 299, sagittal 180; PAT: horizontal 303, sagittal 180; α*-optimal*:

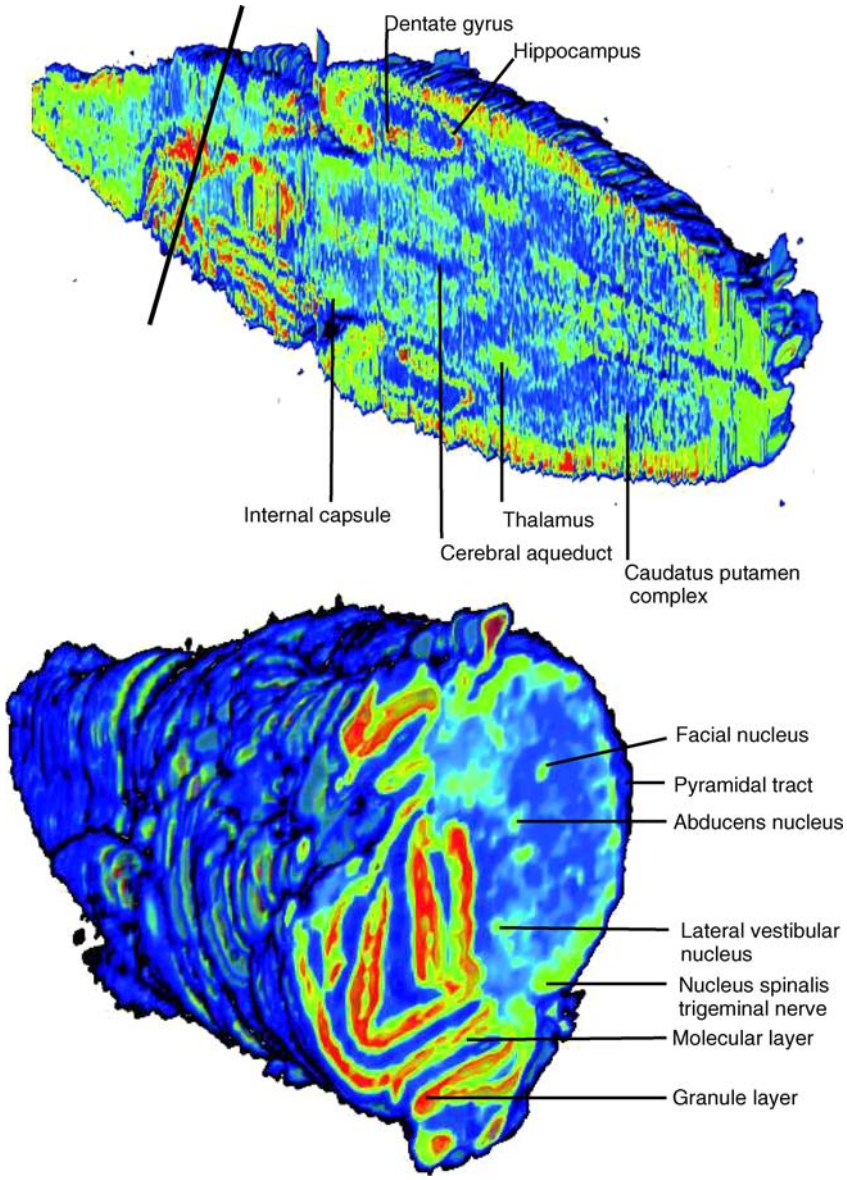

Figure 10. Isoplanar sections through 3D-reconstructions visualized with a colored look-up-map. The black line in the panel above indicates the view on a section of the reconstruction below. This section contains the data of one original image.

horizontal 303, sagittal 180; *partial-optimal*: horizontal 299, sagittal 165). Here, the original stacked images and the PAT images share the same section number and can be compared directly. Note, the original non-registered stacked images cannot be used. An isoplanar section in the PAT image looks more like the isoplanar section in the α-*optimal* result than in the *partial-optimal* reconstructed result. However, we tried to choose isoplanar sections which are as similar as possible.

At last the 3D-reconstruction of a 512×512 pixels large resampled stack of images is reproduced in Fig. 11. In the same figure, we have also reconstructed the same stack of images at original resolution of 6.35 μm edge length of each pixel. The first rostral sections of the olfactory bulb are misregistered because we applied a smaller opening filter (5×5) in order to preserve finer details at such a high resolution. Despite the fact that we applied the robust PAT registration strategy, the sections are not aligned optimally.

Figure 11. The best quality of registration was obtained by the *partial-optimal* approach (upper panel: registration and reconstruction of low resolution images). Therefore, the whole stack of images was registered *partial-optimal* at the original relative large resolution. The resulting reconstruction is shown in the lower panel.

This is because small preserved artifacts around foreground objects which do not pertain to the class of artifacts posses only small masses in comparison to other structures. Hence, they gain a stronger influence on the center of mass and the orientation of the principal axes. Nevertheless, those sections which possesses large masses show an optimal affine alignment result. Interestingly, one can recognize the granule cell layer of the main olfactory bulb which cannot be detected in the reconstruction of the image of lower resolution (same Fig. 11).

3.2. Elastic Registration of the Rat Brain

The *SSD* of the preregistered rat brain images decreases from 281373 (59%) to 229576 (67%) in comparison with the nonregistered images. After 10 steps of elastic registration were performed we observed the largest increase of *SSD*. From 20 to 40 further registration steps the *SSD*s diminishes to 204241, i.e. 70%. The elastic registration of preprocessed but not preregistered images yields to a decrease after 40 steps of the *SSD* to 422969 (38%), only. This means that affine linear

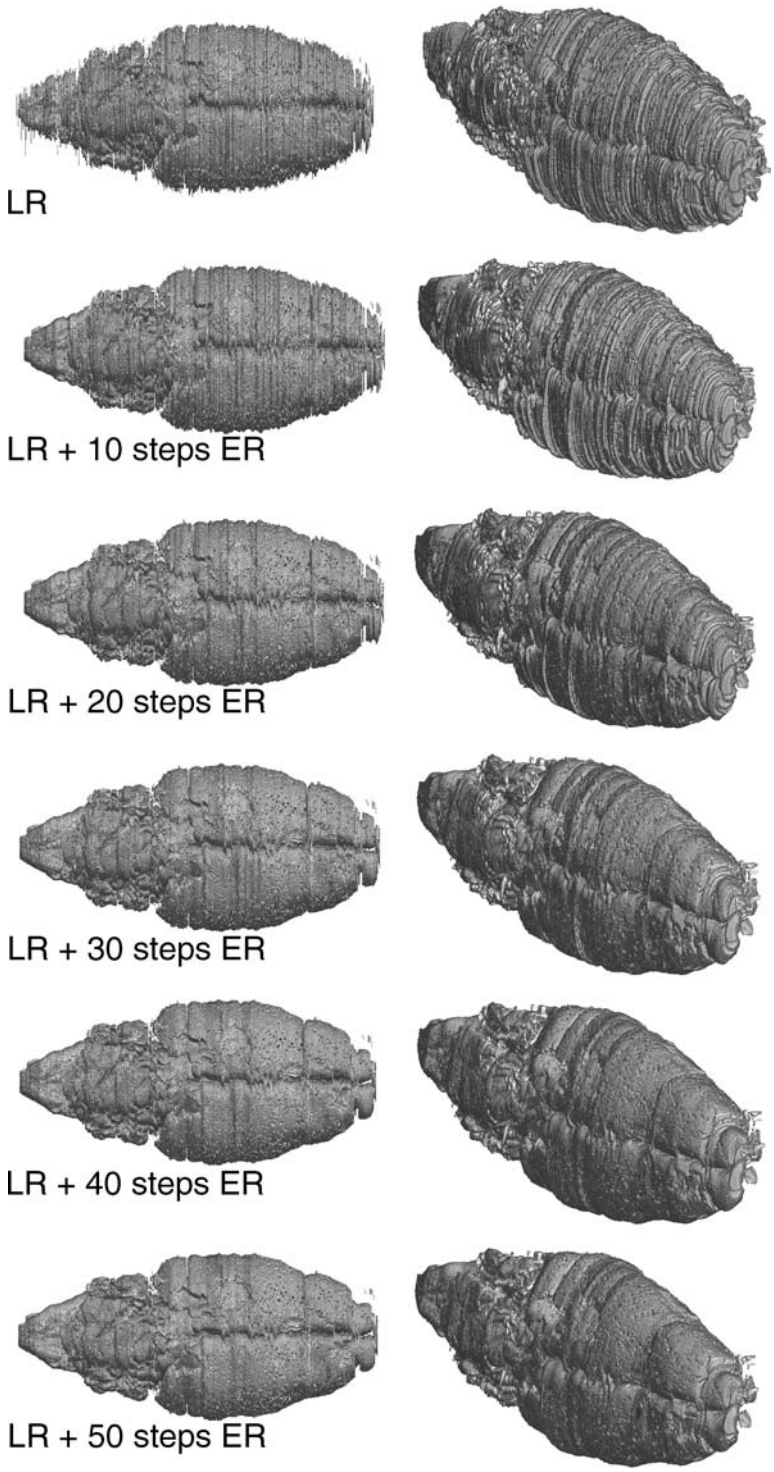

Figure 12. The 3D-reconstructions of the rat brain after affine linear registration (LR) and affine linear with subsequent elastic registration (ER) after 10 to 50 registration steps. Two different projections are shown here: from above (left column) and oblique from the rostral perspective (right column). The smoothness of the surface of the reconstructed brain is correlated with the number of registration steps.

preregistration is essential with respect to quality, quantity and computing time optimization. The 3D-reconstructed rat brain is shown in Fig. 12 after 10 to 40 elastic registration steps and after affine linear registration, only. In the following these results have been applied to the images of the histologic sections of the human forebrain. For the purpose of visualizing some subcortical structures which are investigated often in neuroscience two horizontal sections through the 3D-reconstructed volume are presented in Fig. 13. Especially, the internal capsule, substantia nigra, subthalamic nucleus and the subiculum can be recognized in the reconstruction.

3.3. Registration of the human brain

The paraffine embedded human brain was sectioned resulting in 6214 images. Before sectioning, an episcopic image of the surface of the wax block was produced (Fig. 15(b)). 1.64% (102) of these sections were lost within tissue processing. 450 of the 6112 sections were resampled and registered using the elastic registration method. The registration was performed on a high performance computer cluster (Fig. 14(d)). The run time of the sequential version of the elastic registration of two 512×512 pixel images is about 100 minutes whereby the parallel computation on the 48 dual pentium node cluster lasts 188 seconds. This means that the parallel implementation on the high performance cluster needs for 100 images (512×512 pixel) about 5.22 hours. In comparison to the serial version of the elastic registration algorithm this is a speed up of 96.9%.

The elastic registration of the same 21 images (1024×1024 of the rat brain that were used for computing-time measurements within the affine linear approach lasted in average 3.34 hours on a 1 GHz Pentium III computer. If these images were preprocessed only but not preregistered by the affine linear approach the computing-time increases up to 7.87 hours in average.

Comparing the (linearly corrected) template 117 with the reference image 116 shows a difference of $||T - R|| \approx 10361$ in the Frobenius norm. Using our elastic matching algorithm, we are able to reduce the difference to $||T_{200} - R|| \approx 3123$, which is ca. 30.1% of the initial difference. Here, we performed 200 iteration steps until 30.1% were reached.

The four different perspectives to 3D-reconstructions of these sections which are lying within the occipital lobes are shown in (Fig. 18). In these 3D-reconstructions the sulcus calcarinus can be detected easily. The stripe of Gennari, i.e. lamina IVb, is visualized in a horizontal isoplanar section

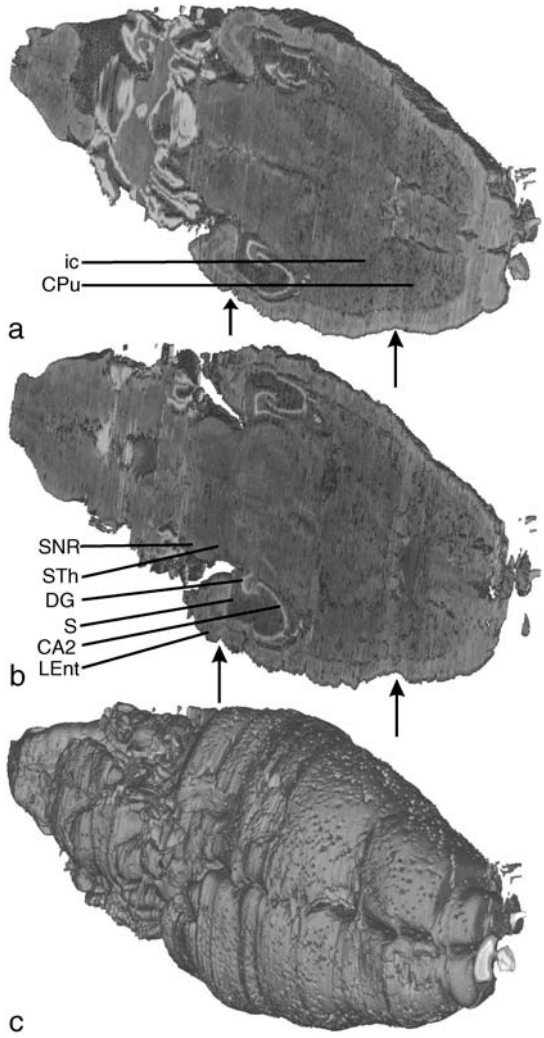

Figure 13. Within two horizontal planes through the reconstructed brain volume some structures of interest can be recognized now which are not visible without registration, i.e. ic: internal capsule, CPu: caudate putamen complex, SNR: substantia nigra, STh: subthalamic nucleus, DG: dentate gyrus, S: subiculum, CA2: field CA2 of hippocampus, LEnt: lateral enthorinal cortex. (a) horizontal section on the level of the olfactory bulb. (b) horizontal section below the olfactory bulb. (c) Smoothed 3D-reconstruction of the elastic registered sections after 40 registration steps. The latter reconstruction is shown from the same viewpoint like horizontal sections in (a) and (b). The arrows are pointing to dents in the surface of the brain. They can be observed within intramodal registration if loss of tissue inside the biologic object occur.

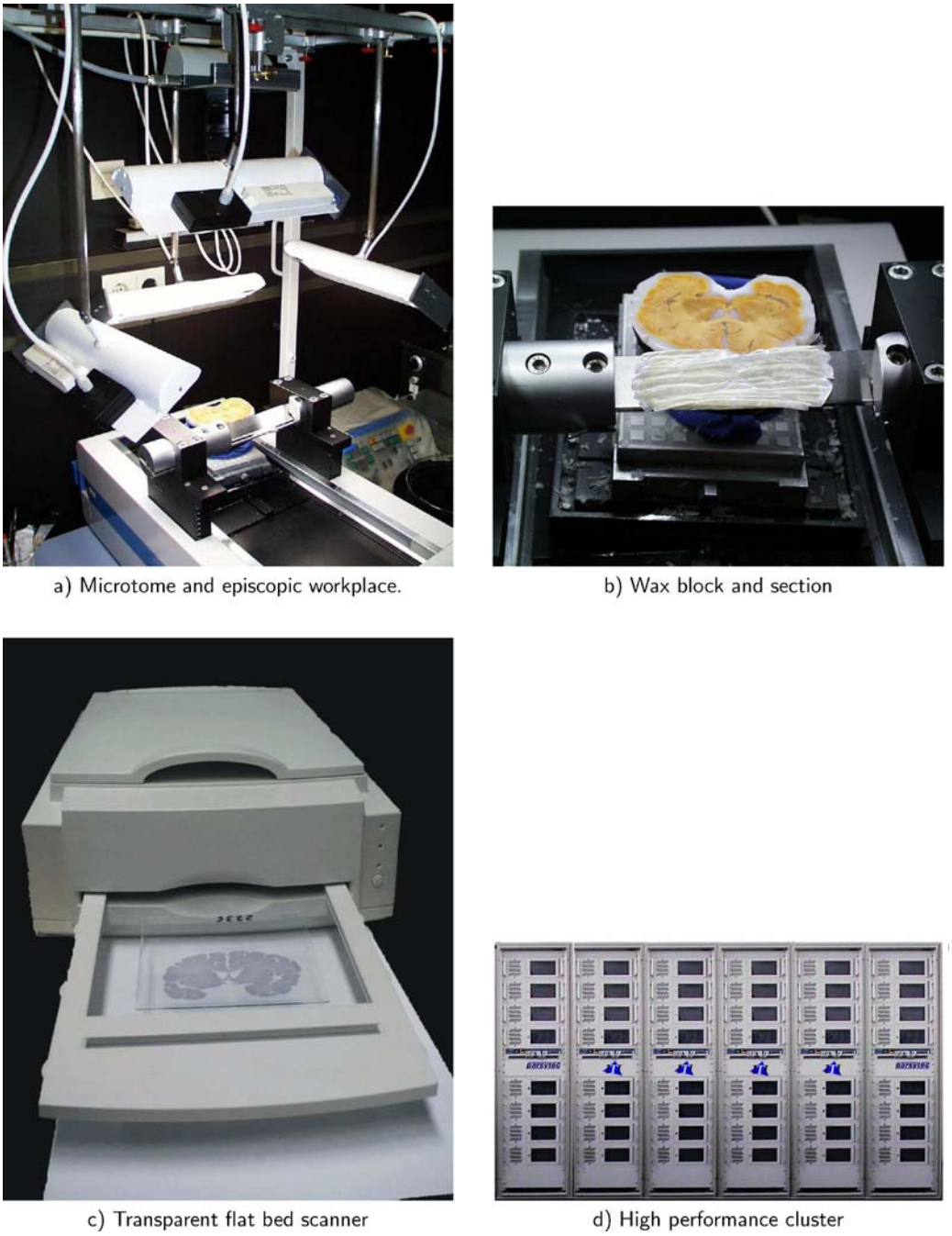

Figure 14. The sliding microtome with the scanner camera that have been used for digitizing each paraffin wax block surface before the next section have been produced (a), a deformed 20 μm section on the knife of a microtome (b), a large histologic section on the high resolution transparent flat bed scanner (c), the high performance computer cluster with 48 dual PII processors (d).

through the 3d-reconstruction (Fig. 19). The neuron poor lamina IVb can be seen better in area 17 of the right occipital lobe. Gyral structures that have been sectioned tangentially and are not connected to the tissue object with the largest area of all tissue objects in an image were matched in correct topographic relation.

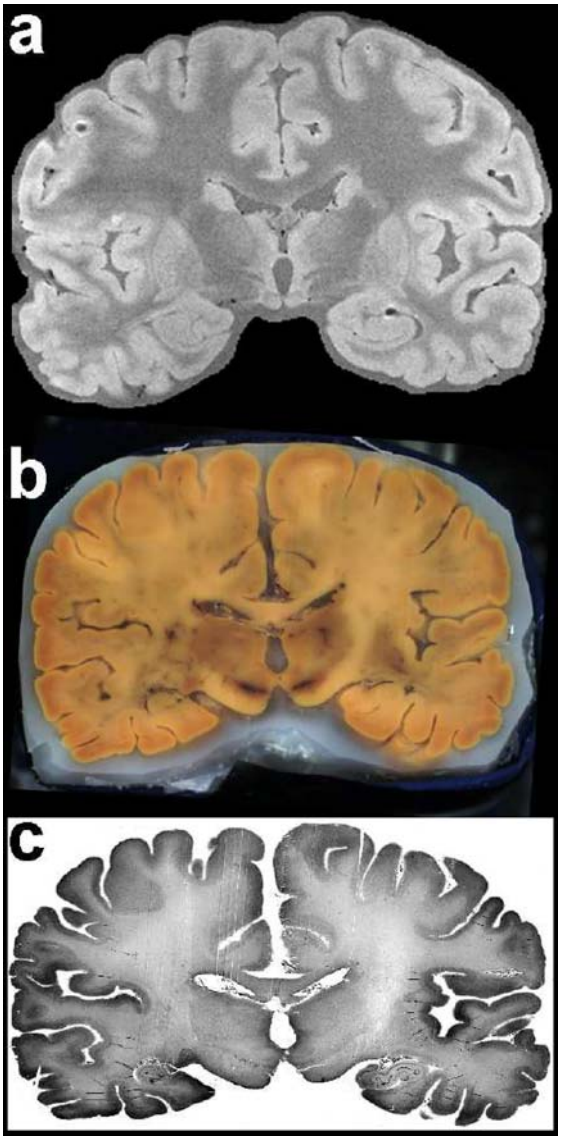

Figure 15. (a) The brain that have been processed was evaluated by an MRI-scanner (MRI-modality). (b) Paraffin wax surfaces were digitized before each sectioning process (episcopic modality). (c) High resolution flat bed scan images were produced from each histologic section of the investigated brain (FBS modality).

Finally, we have used the force fields calculated by the elastic registration algorithm in order to determine in four consecutive sections (116 to 119) the exact centers of gravitation of each neuron (Fig. 20). The gravitation centers have been detected before by a image analytical procedure described by Schmitt et al. (2005). The registration of the gravitation centers of the detected cells and reconstruction is shown in Fig. 21. The cortex, lamina I and II as well as the white matter border can be detected easily in the registered object data.

4. Discussion

4.1. The Registration Chain: From Affine to Elastic

The result of the proposed approach of robust affine linear registration is a reliable alignment of histologic sections of a whole brain of a rat that shows in 3D-reconstructions structures which were not visible before registration. The robustness of the algorithm that was implemented is an outstanding feature in regard to the alignment of histologic material. Because it has a very low sensitivity to noise we will use it for a fast pre-registration. The pre-aligned images are a promising starting point for a consecutive nonlinear registration which will spend less computing time than without pre-registration because the convergence will be reached sooner.

4.2. The Affine Linear Approaches

We have presented different approaches to affine linear registration. Because the standard PAT of *histologic* images leads to unwanted trends in the registration result, we must recommend our robust version. Prior studies describe other algorithms which were developed for rigid transformations (Kuglin and Hines, 1975; de Castro and Morandi, 1987; Hibbard et al., 1992; Zhao et al., 1993; Alexander et al., 1997). However, these approaches are not as flexible as the technique investigated here with respect to subsequent optimizations. These optimizations may concern the translation (2 parameters), the rotation (1 parameter) and the shearing (1 parameter) as well as the scaling (2 parameter). Applying optimization of the first three components (translation, rotation, shear) leads to smoother surfaces in the 3D-reconstructions and to the smallest *SSD*. Finer details, convexities and concavities are preserved. Recently, Arsigny et al. (2005) developed a polyrigid and polyaffine transformation that was applied sucessfully to histologic sections.

As explicated before, affine linear registration of foreground structures in stacks of images are aligned in reference to their centroids. These centroids are spatial points of convergence of the foreground structures.

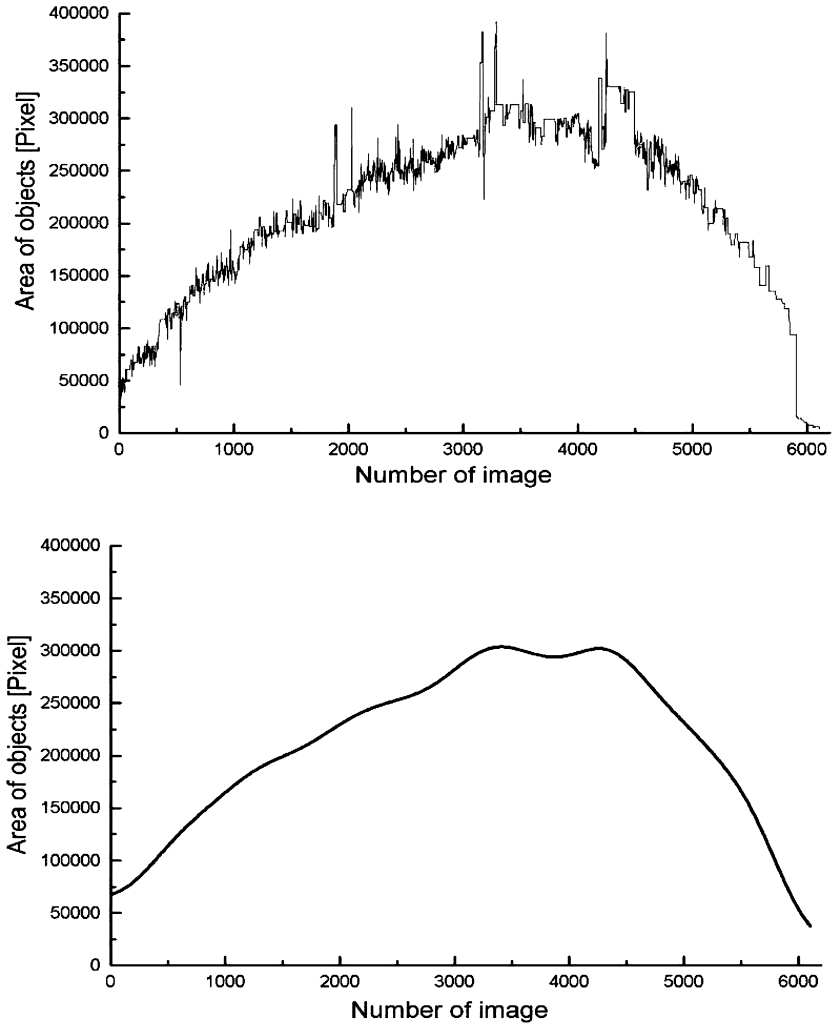

Figure 16. Top: The size of the foreground (ordinate) within each image of the whole series of digitizes histologic sections (abscissa) of the human forebrain is presented here. Below: In this diagram the smoothed distribution of foreground areas is shown. In the left part of this diagram section size increases slower (frontal lobe) whereby on the right side the decrease of section size is stronger within the parietal and occipital lobe.

Since no external references (e.g. fiducial markers) were used in this kind of registration it is more likely that sections through a curved cylinder converge to a tube like object after reconstruction (Fig. 5).

Scaling optimization was not considered here because all images are digitized at the same magnification and resolution. Moreover, deformations effecting the scaling or larger local volume bulges of the brain do not appear. However, scaling have to be kept in mind because single sections may be compressed also and therefore need to be registered in respect of scaling. Since now, we are not able to recommend an affine linear method or a nonlinear method to align distortions due to compression or dilation.

These observations suggest that, compared to other algorithms, e.g. chamfer matching (You, 1995; Borgefors, 1988), fiducial markers (Ongaro et al., 1991; Maurer et al., 1997; Kremser et al., 1997; de Munck et al., 1998; West et al., 2001) and other implementations (Ozturk, 2002; Woods, 2002), our robust rigid registration combined with affine linear optimization of translation, rotation and shearing lead to an optimal starting point for a succeeding nonlinear registration technique.

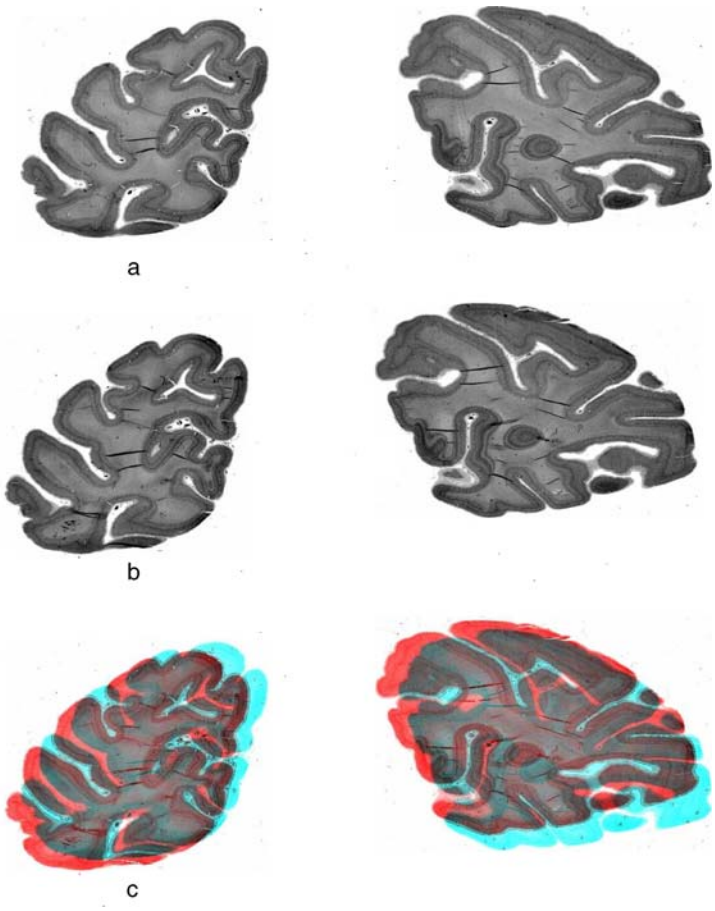

Figure 17. A template image (T) of a section (above) and a reference image (R) of a consecutive section (middle) are shown. The foreground objects, i.e. views of the occipital lobes) in the images do not match exactly (below).

Ourselin and coauthors (Ourselin et al., 2001b) investigated registration robustness of comparable material as done here. They have shown by a new sophisticated approach the *block matching algorithm* applied to digitized histologic images that have to be registered and using the correlation coefficient as an appropriate similarity measure satisfying reconstructions can be obtained. They used a robust estimate, the convex M-estimator or L_1-estimator that is suitable for point matching to generate reliable results. So far, we do not have implemented this technique which is of interest for comparison of robustness issues.

As elaborated by Schormann and Zilles (1997) and Schormann et al. (1997) minute shearing results in strong rotational errors if the shapes are approximately square, but scaling errors dominate in cases with extensive shearing can be minimized by combine the robust PAT approach introduced here by consecutive affine optimizations. Small misalignments of adjacent sections can be corrected much faster by an elastic method after preregistration with the robust *partial-optimal* technique than direct by the elastic approach because the extension of mismatch was previously reduced. Furthermore, affine preregistration before elastic registration may have a direct qualitative effect of preserving the morphology of the histologic structures. If the global deformation components like translation, rotation and shearing are registered primary local by a nonlinear approach local deformations can be introduced into the resulting images.

We must emphasize that the *partial-optimal* approach is a necessary initial registration procedure. However, an affine linear model is not

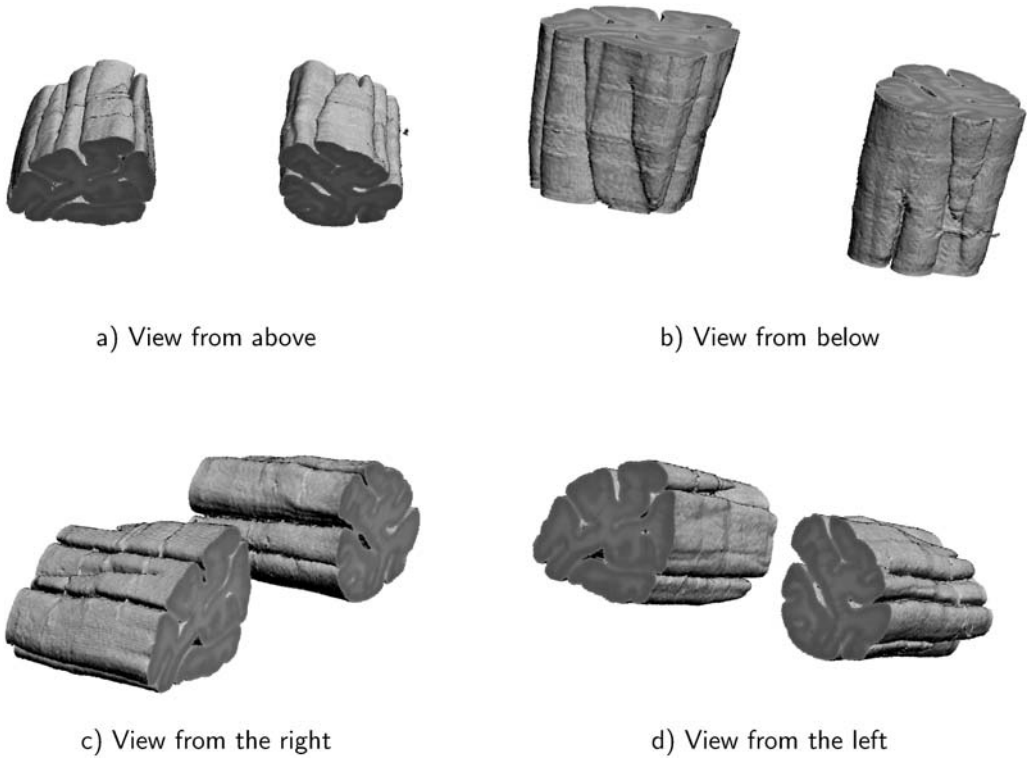

Figure 18. 3D-reconstructions of the elastic registered images 100 to 199. Here, four different views to the reconstructed stack of images are presented.

sufficient to register images that contain nonlinear deformations. Therefore, it is indispensable to align images of serial histologic sections in a multiresolution-multiregistration framework for a best possible correction of deformations.

4.3. Elastic Registration and Megapixel Images

After pre-alignment the images still contain deformations (Fig. 9(c)) that are local and nonlinear. Such local deformations are getting more important if images of histologic sections with high resolution up to a coarse cellular presentation are registered. So far we are not able to determine if the remaining deformations are attributed to small affine linear distortions. Nevertheless, the affine linear pre-alignment have reached an optimum. Therefore, a local nonlinear technique like elastic registration is an inevitable procedure for a consequent final alignment of histologic images.

The theoretical framework of elastic registration has been published first 20 years ago by (Broit, 1981; Bajcsy, 1982; Bajcsy, 1983; Bajcsy and Kovačíč, 1989). This kind of local and nonlinear intensity based registration was applied to histologic sections (Schormann, 1996; Schormann and Zilles, 1998) intramodal (MRI to MRI) and intermodal (histologic to MRI). Some subsequent works about nonlinear registration of inter- and intramodal elastic alignment where histologic image data were involved have been published by Mega et al. (1997), Cohen et al. (1998), Jacobs et al. (1999), Bardinet et al. (2001), Toga and Thompson (2001) and Ourselin et al. (2001a,b). However, in these works no high resolution image data are used and no computing optimizations were realized. Therefore, we have developed a parallel implementation of a fast solver of the equation systems to maintain the force fields and the results of our nonlinear approach are presented here for the first time.

In comparison to other elasticity based registrations of MRI, PET or other material (Davatzikos, 1997; Ashburner et al., 2000; Hayakawa et al., 2000; Iosifescu et al., 1997; Ferrant et al., 2001; Guimond et al., 2001; Christensen and Johnson, 2001; Christensen

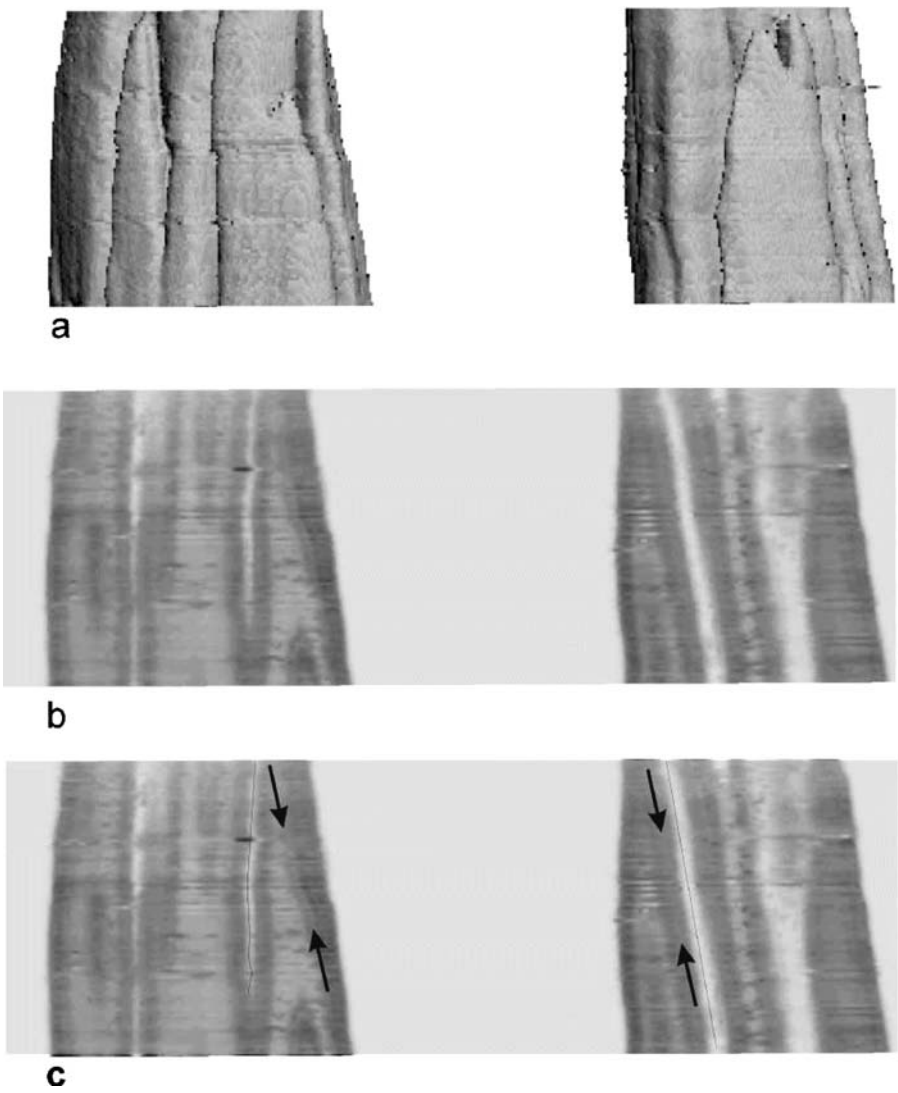

Figure 19. On top the perspective on the 3D-reconstruction form above is displayed. A virtual section through the 3D-reconstruction has been performed. In the isoplanar view somebody can detect the stripe of Gennari (arrows) within area 17 and the calcanear sulus (black lines).

et al., 1997; du Bois d'Aische et al., 2005; Auer et al., 2005) we are working with very large images of up to 11000×7000 ($= 77 \times 10^6$) pixels. The resulting system of linear equations has a size of $1.40612164 \times 10^{32}$ ($= 4 \times n^4$). Therefore, Fischer and Modersitzki (1999, 2001) developed a superfast direct solution scheme (full multigrid), based on the Fast Fourier Transformation. In addition, this solution scheme has been implemented on a high performance computer cluster. An alternative would be solving the equation system by a parallelized additive operator splitting (AOS) technique or parallelized multigrid computing (Thompson and Ferziger, 1989; Vatsa and Wedan, 1990; Schieweck, 1993; Webster, 1994).

4.4. Nonlinear Registration Alternatives to the Elastic Approach

An alternative to the elastic approach would be thin plate splines with landmarks (Bookstein, 1984, 1989; Davatzikos and Prince, 1994; Davatzikos, 1997; Maurer et al., 1997; Rangarajan et al., 1997; Baheerathan et al., 1998; Cohen et al., 1998; Gold et al.,

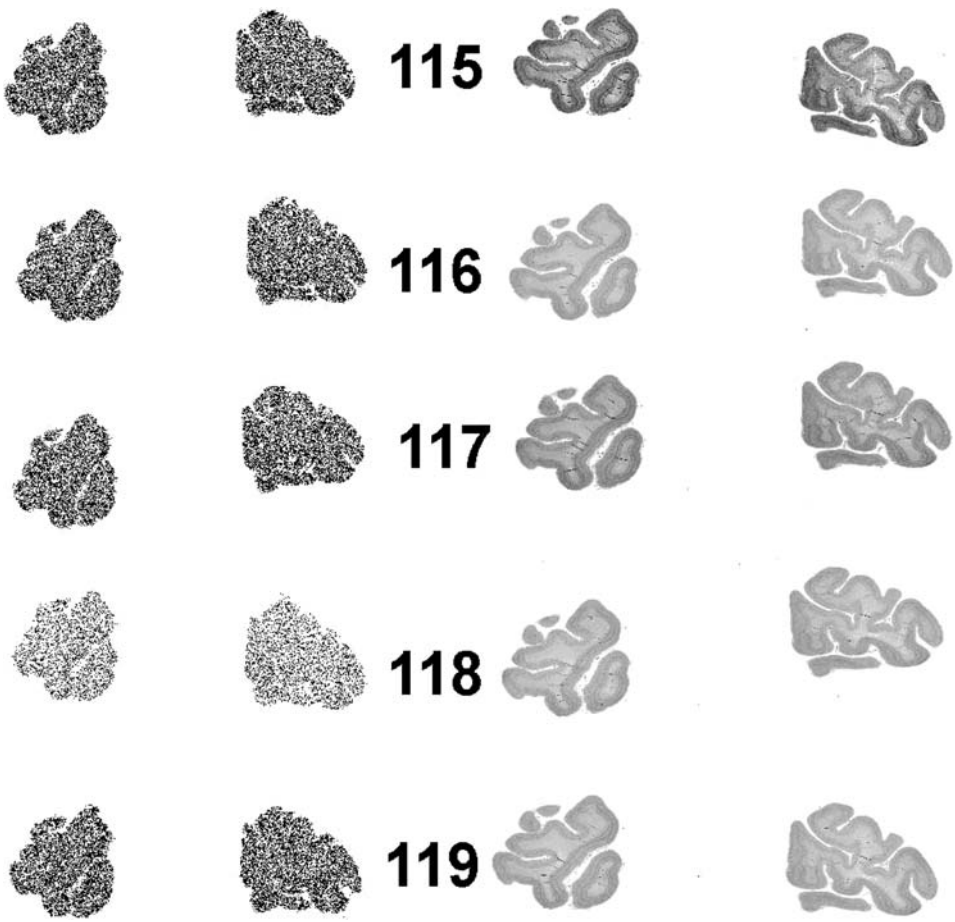

Figure 20. Within section 115 to 119 each cell was detected. Each 40th cell has been plotted on the left side of this plate. The corresponding FBS-image is shown on the right. Section 118 was slightly thinner. Therefore, we found fewer cells within the section space.

1998; Kostelec et al., 1998; Rangarajan et al., 1999; Joshi and Miller, 2000; Chui et al., 2001; Johnson and Christensen, 2001; Rohr et al., 2001), trilinear Bézier splines (B-splines) (Rueckert et al., 1999; Otte, 2001), nonlinear registration via genetic algorithms (Rouet et al., 2000) or deformable organisms (autonomous agents) derived from artificial life computing concepts (Hamilton et al., 2001). However, landmarks have to be determined *exactly* which could be a limiting factor for very complex series of images (Collins et al., 1995; Likar and Pernus, 1999; MacDonald et al., 2000). Other non-linear methods like optical flow (Horn and Schunck, 1981; Hellier et al., 2001) and fluid dynamic models (Christensen, 1994; Christensen et al., 1997; Lester and Arridge, 1999; Christensen and Johnson, 2001) which are applied for matching images of different modalities or between different individuals have to many degrees of freedom. This could lead to problems at those parts of images were loss of tissue or larger cracks and crinkles are present. Furthermore, the physical effects which introduce deformations consists of extension (dilatation) and tension (contraction) forces and not of movement artifacts (optical flow) or applying a registration task to images which are derived from different physical devices or which should be registered to different individuals.

4.5. Similarity Measures

In our approach of elastic registration only one distance measure was applied. According to Penney et al. (1998), Studholme et al. (1999), Holden et al. (2000) and Zhu (2002) other measures of similarity

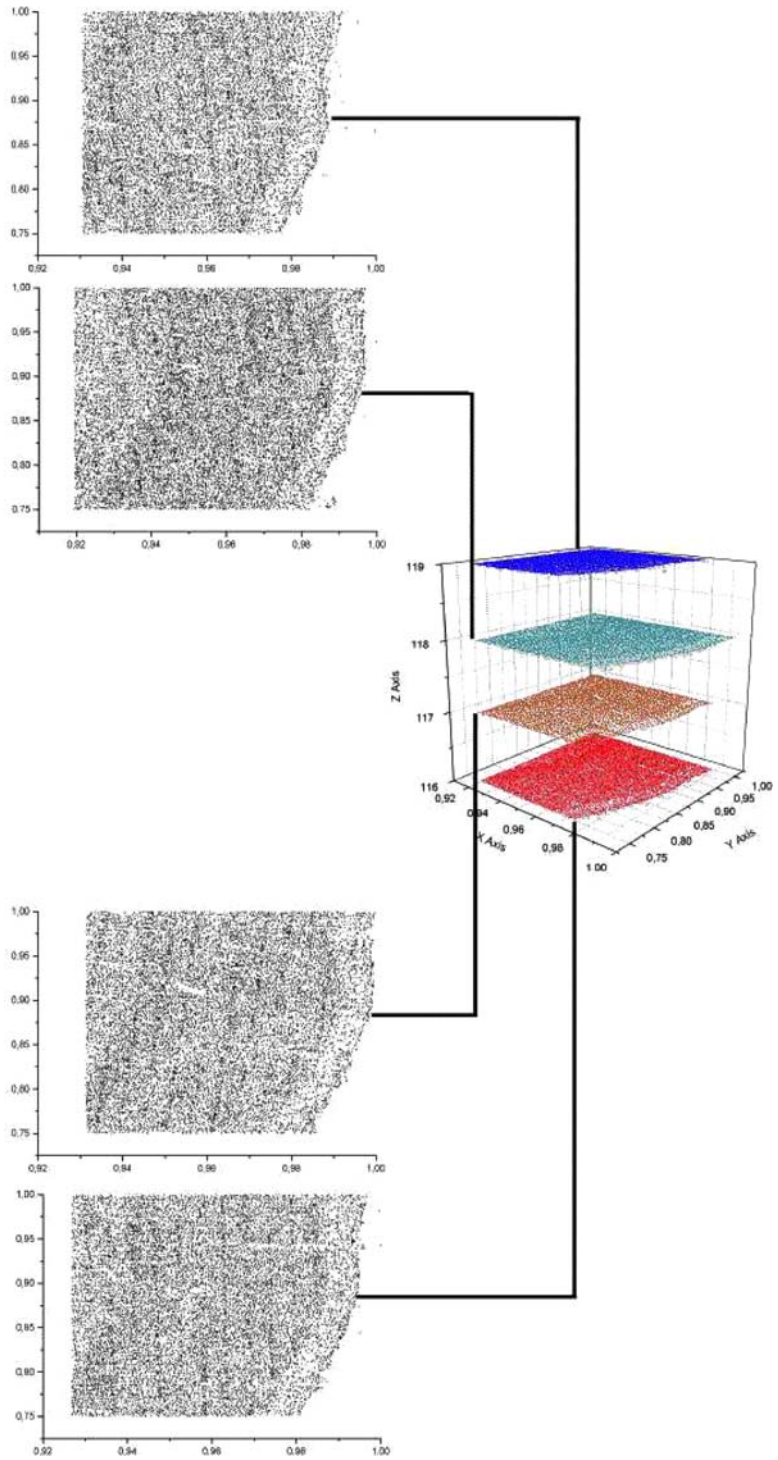

Figure 21. A region of interest of the object data was aligned using the result of the elastic registration of FBS-images 116 to 119. Laminar details and the white matter border can be detected in the plots of each gravitation center of the cells. On the right we have plotted the 3D-particle space of the aligned object data.

can be used too. Therefore, we will investigate further similarity measures.

4.6. Drawbacks

Rohlfing and Maurer (2001) pointed out that the volume of contrast-enhancing structures are decrease after elastic registration. This effect can be reduced by an incompressibility constraint approach based on the Jacobian determinant of the deformation that can be computed rapidly. Such a constrained elastic registration have to be tested on our image material. If this approach would preserve fine contrast details of the laminar structure then we would be able to analyze the lamination pattern of the cortex in three dimensions.

Since now, the images of the histologic sections were not registered bimodaly to a reference data set that can be obtained from MRI. A further approach was published by Gefen et al. (2003) who developed registration of a rat brain to internal and external surfaces serving as guides or surface references. An intrasubject reference of the rat brain used here is not available. Nevertheless, the intramodal elastic registration decreases the *SSD* and increases the quality of the reconstructed morphology. The arrows in Fig. 13 are pointing to dents of the rat brain surface which do not occur normally. If sections with some loss of tissue inside the brain are registered the image structures can be pulled more and more inside the volume in order to minimize the *SSD*. This can be prevented by a bimodal registration of the histologic data set to a prehistologic MRI-dataset of the same biologic object.

4.7. Other Applications

Nonlinear registration schemes (elastic solid, fluid viscous, mutual information, optical flow) are the scaffolding for co-registration and multimodal registration strategies that are used for atlas development (Thurfjell et al., 1995; Toga et al., 1995; Nowinski et al., 1997; McInerney and Roberts, 1998; Juan et al., 2000; Nowinski and Thirunavuukarasuu, 2001), computer aided surgery (Maurer et al., 1998a,b,c; Woods et al., 1999; Jannin et al., 2000; Rohlfing et al., 2000; Murphy et al., 2001; Mutic et al., 2001; Watanabe et al., 2001; Sabbah et al., 2002) and structure-function-data correlation investigations (Mega et al., 1997; Viergever et al., 1997). Multimodal registrations deliver objective approaches that enable easy and intuitive image registration. This can be of great help for the physician who arrive at more optimal diagnoses and better treatment decisions. Beside the development of atlases for surgery tasks nonlinear registration, in particular fluid models with more degrees of freedom, is essential for matching single subject data sets to group data sets for evaluation and comparison of macroscopic brain similarities as well as differences (Santori and Toga, 1993).

4.8. AIR

The registration software package AIR 5.06 (Woods et al., 1998a,b) (`http://128.97.134.164/AIR5/index.html`) is able to perform affine linear and nonlinear registrations as well as co-registrations (Kiebel et al., 1997). However, as already shown by Hsu et al. (2001), registration results can be enhanced by other methods and modifications.

4.9. Closing Words

Elastic registration of high resolution images of serial histologic sections of the human brain is quantitatively accurate and provides an registered stack of images that can be directly reconstructed and rendered. The reconstructions, once completed, offers insights into the spatial arrangement of morphologic entities like different cortical regions, laminae, subcortical nuclei and fiber tracts which are the origin for exact 3D cellular object reconstructions as shown exemplary. Therefore, we are confident to apply this introduced, modified and successful tested registration framework from the preprocessing over affine and elastic alignment to 3D-reconstruction and rendering to the whole high resolution data set of over 6000 sections of a human brain.

Acknowledgments

We thank U. Almert, P. Lau, E. Mecke of the Institute of Anatomy (University of Lübeck) for their excellent histologic preparations, digitizing and data administration, W. Kühnel and J. Westermann (Institute of Anatomy, University of Lübeck) for their extensive support, S. Prehn (Institute of Technical Informatics, University of Lübeck) for optimizing and administration the SF 15K computer on which several computing experiments were performed. We are indebted to Prof. Dr. Lutz Dümbgen for valuable

comments and helpful discussions concerning the stochastic questions. We gratefully acknowledge Martin Böhme and Susanne Bock for programming graphical user interfaces. Furthermore, we have to express our gratitude to A. Wree (Institute of Anatomy, University Rostock) for his important suggestions and critical discussion of this study. M. Westlund was of great help editing and correcting the manuscript. This work was supported by the Gerhard Ten Doornkaat Koolman foundation and the Possehl foundation.

References

Abbe, E. 1873. Beiträge zur Theorie des Mikroskops und der mikroskopischen Wahrnehmung. *Arch. Mikr. Anat.*, 9:413.

Abeles, M. 1991, *Corticonics. Neural circuits of the cerebral cortex*. Cambridge University Press: Cambridge.

Aferzon, J., Chau, R., and Cowan, D. 1991. A microcomputer-based system for three-dimensional reconstructions from tomographic or histologic sections. *Anal. Quant. Cytol. Histol.*, 13:80–88.

Alexander, M., Scarth, G., and Somorjai, R. 1997. An improved robust hierarchical registration algorithm. *Magn. Reson. Imaging.*, 15:505–514.

Alpert, N., Bradshaw, J., Kennedy, D., and Correia, J. 1990. The principal axes transformation—a method for image registration. *J. Nuc. Med.*, 31:1717–1722.

Amit, Y., Grenander, U., and Piccioni, M. 1991. Structural image restoration through deformable templates. *J. Am. Stat. Ass.*, 86:376–387.

Arbib, M. 1995, *The Handbook of Brain Theory and Neural Networks*. MIT Press: Cambridge.

Arsigny, V., Pennec, X., and Ayache, N. 2005. Polyrigid and polyaffine transformations: A novel geometrical tool to deal with non-rigid deformations—Application to the registration of histological slices. *Med. Image. Anal.*, 9:507–523.

Ashburner, J., Andersson, J., and Friston, K. 2000. Image registration using a symmetric prior–in three dimensions. *Hum. Brain. Mapp.*, 9:212–225.

Auer, M., Regitnig, P., and Holzapfel, G. 2005. An automatic nonrigid registration for stained histologic sections. *IEEE Trans. Imag. Proc.*, 14:475–486.

Baheerathan, S., Albregtsen, F., and Danielsen, H. 1998. Registration of serial sections of mouse liver cell nuclei. *J. Microsc.*, 192:37–53.

Bajcsy, R. 1982. Matching of deformed images. *Proc. 6th Int. Conf. Patt. Recogn.*, 6:351–353.

Bajcsy, R. 1983. A computerized system for the elastic matching of deformed radiographic images to idealized atlas images. *J. Comp. Ass. Tomo.*, 7:618–625.

Bajcsy, R. and Kovačíč, S. 1989. Multiresolution elastic matching. *Comp. Vis. Image. Proc.*, 46:1–21.

Banerjee, P. and Toga, A. 1994. Image alignment by integrated rotational and translational transformation matrix. *Phys. Med. Biol.*, 39:1969–1988.

Bardinet, E., Colchester, A., Roche, A., Zhu, Y., He, Y., Ourselin, S., Nailon, B., Hojjat, S., Ironside, J., Al-Sarraj, S., Ayache, N., and Wardlaw, J. 2001. Registration of reconstructed post mortem optical data with MR scans of the same patient. *LNCS*, 2208:957–965.

Barnard, S. and Thompson, W. 1980. Disparity analysis of images. *IEEE Trans. PAMI*, 2:333–340.

Barnea, D. and Silverman, H. 1972. A class of algorithms for fast digital image registration. *IEEE Trans. Comp.*, 21:179–186.

Baumann, M. and Scharf, H. 1994. Moderne Bildverarbeitungsverfahren als Unterstützung der räumlichen Rekonstruktion histologischer Strukturen. *Ann. Anat.*, 176:185–188.

Benveniste, H. and Blackband, S. 2002. MR microscopy and high resolution small animal MRI: Applications in neuroscience research. *Prog. Neurobiol.*, 67:393–420.

Böhme, M., Hagenau, R., Modersitzki, J., and Siebert, B. 2002. Nonlinear image registration on PC-clusters using parallel FFT techniques. Technical Report SIIM-TR-A-02-08, Institute of Mathematics, Medical University of Lübeck.

Bookstein, F. 1984. A statistical method for biological shape comparisons. *J. Theor. Biol.*, 107:475–520.

Bookstein, F. 1989. Principal warps: Thin-plate splines and the decomposition of deformations. *IEEE Trans. Patt. Anal. Mach. Intell.*, 11:567–585.

Borgefors, G. 1988. Hierarchical chamfer matching: A parametric edge matching algorithm. *IEEE Trans. PAMI*, 10:849–865.

Born, G. 1883. Die Plattenmodellirungsmethode. *Arch. Mikr. Anat.*, 22:584–599.

Braitenberg, V. 1978. Cell assemblies in the cerebral cortex. *Lec. Notes. Biomath.*, 21:171–188.

Bro-Nielsen, M. and Gramkow, C. 1996. Fast fluid registration of medical images. *LNCS*, 1131:267–276.

Broit, C. 1981. Optimal registration of deformed images. Ph.D. thesis, Computer and Information science, University of Pensylvania.

Bron, C., Launay, D., Jourlin, M., Gautschi, H., Bächi, T., and Schüpbach, J. 1990. Three dimensional electron microscopy of entire cell. *J. Mircosc.*, 157:115–126.

Brown, L. 1992. A survey of image registration techniques. *ACM Comp. Surv.*, 24:325–376.

Budo, A. 1990, *Theoretische Mechanik*. VEB Deutscher Verlag der Wissenschaften.

Christensen, G. 1994. Deformable shape models for anatomy. Ph.D. thesis, Sever Institute of Technology, Washington University.

Christensen, G. and Johnson, H. 2001. Consistent image registration. *IEEE Trans. Med. Imaging.*, 20:568–582.

Christensen, G., Joshi, S., and Miller, M. 1997. Volumetric transformation of brain anatomy. *IEEE Trans. Med. Imaging.*, 16:864–877.

Chui, H., Win, L., Schultz, E., Duncan, J., and Rangarajan, A. 2001. A unified feature registration method for brain mapping. *LNCS*, 2082:300–314.

Ciarlet, P. 2000. *Mathematical Elasticity*. Elsevier Science.

Cohen, F., Yang, Z., Huang, Z., and Nissanov, J. 1998. Automatic matching of homologous histological sections. *IEEE Trans. Biomed. Eng.*, 45:642–649.

Collins, D., Holmes, C., Peters, H., and Evans, A. 1995. Automatic 3D model-based neuroanatomical segmentation. *Hum. Brain. Mapp.*, 3:190–208.

Dauguet, J., Mangin, J.-F., Delzescaux, T., and Frouin, V. 2004. Robust inter-slice intensity normalization using histogram scale-space analysis. *LNCS*, 3216:242–249.

Davatzikos, C. 1997. Spatial transformation and registration of brain images using elastically deformable models. *Comput. Vis. Image. Underst.*, 66:207–222.

Davatzikos, C. and Prince, J. 1994. Brain image registration based on curve mapping. *Proc. IEEE Workshop. Biom. Image. Anal.*, 245–254.

de Castro, E. and Morandi, C. 1987. Registration of translated and rotated images using finite Fourier transforms. *IEEE Trans. PAMI*, 9:700–703.

de Munck, J., Verster, F., Dubois, E., Habraken, J., Boltjes, B., Claus, J., and van Herk, M. 1998. Registration of MR and SPECT without using external fiducial markers. *Phys. Med. Biol.*, 43:1255–1269.

Desgeorges, M., Derosier, C., Cordoliani, Y., Traina, M., de Soultrait, F., Bernard, C., Khadiri, M., and Debono, B. 1997. Imaging networks, surgical simulation, computer-assisted neurosurgery. *J. Neuroradiol.*, 24:108–115.

Dierker, M. 1976, *An Algorithm for the Alignment of Serial Sections*. John Wiley & Sons: New York, P.B. Brown: Computer technology on neuroscience edition.

Dougherty, E. 1993, *Mathematical Morphology in Image Processing*. Marcel Dekker: New York, Basel, Hong Kong.

du Bois d'Aische, A., Craene, M. D., Geets, X., Gregoire, V., Macq, B., and Warfield, S. 2005. Efficient multi-modal dense field non-rigid registration: Alignment of histological and section images. *Med. Image. Anal.*, 9:538–546.

Ferrant, M., Nabavi, A., Macq, B., Jolesz, F., Kikinis, R., and Warfield, S. 2001. Registration of 3-D intraoperative MR images of the brain using a finite-element biomechanical model. *IEEE Trans. Med. Imaging.*, 20:1384–1397.

Fischer, A. and Modersitzki, J. 1999. Fast inversion of matrices arising in image processing. *Num. Algo.*, 22:1–11.

Fischer, A. and Modersitzki, J. 2001. A super fast registration algorithm. *BVM*, 22:168–173.

Fischer, A. and Modersitzki, J. 2002. Fast diffusion registration. *Contemp. Math.*, 313:117–129.

Fischer, M. and Elschlager, R. 1973. The representation and matching of pictorial structure. *IEEE Trans. Comput.*, 1:67–92.

Fortner. 1999. *User's Guide and Reference Manual*. Fortner Software: Boulder.

Fu, Y. and Ogden, R. 2001. *Nonlinear Elasticity: Theory and Applications*. Cambridge University Press: Cambridge.

Gefen, S., Tretiak, O., and Nissanov, J. 2003. Elastic 3-D alignment of rat brain histological images. *IEEE Trans. Med. Imag.*, 22:1480–1489.

Gerstein, G., Bedenbaugh, P., and Aertsen, A. 1989. Neuronal assemblies. *IEEE Trans. Biomed. Engin.*, 36:4–14.

Glaser, J. and Glaser, M. 1965. A semi-automatic computer-microscope for the analysis of neuronal morphology. *IEEE Trans. Biomed. Eng.*, 12:22–31.

Gold, S., Rangarajan, A., Lu, C., Pappu, S., and Mjolsness, E. 1998. New algorithms for 2-D and 3-D point matching: pose estimation and correspondence. *Pat. Recogn.*, 31:1019–1031.

Golub, G. and van Loan, C. 1989. *Matrix Computations*. Second edition. The John Hopkins University Press: Baltimore.

Green, A. and Adkins, J. 1970. *Large Elastic Deformations*. Clarendon Press: Oxford.

Green, A. and Zerna, W. 1968. *Theoretical Elasticity*. Clarendon Press: Oxford.

Gremillet, P., Bron, C. Jourlin, M., Bachi, T., and Schüpbach, J. 1991. Dedicated image analysis techniques for three-dimensional reconstruction from serial sections in electron microscopy. *Mach. Vis. Appl.*, 4:263–270.

Guimond, A., Roche, A., Ayache, N., and Meunier, J. 2001. Three-dimensional multimodal brain warping using the demons algorithm and adaptive intensity corrections. *IEEE Trans. Med. Imaging.*, 20:58–69.

Hajnal, J., Saeed, N., Soar, E., Oatridge, A., Young, I., and Bydder, G. 1995. A registration and interpolation procedure for subvoxel matching of serially acquired MR images. *J. Comput. Assist. Tomogr.*, 19:289–296.

Hamilton, P., McInerney, T., and Terzopoulos, D. 2001. Deformable organisms for automatic medical image analysis. *LNCS*, 2208:66–76.

Hayakawa, N., Thevenaz, P., Nirkko, A., Uemura, M.U., Ishiwata, K., Shimada, Y., Ogi, N., Nagaoka, T., Toyama, H., Oda, K., Tanaka, A., Endo, K., and Senda, M. 2000. A PET-MRI registration technique for PET studies of the rat brain. *Nucl. Med. Biol.*, 27:121–125.

Hebb, D. 1949, *The Organization of Behavior*. Wiley: New York.

Hellier, P., Barillot, C., Memin, E., and Perez, P. 2001. Hierarchical estimation of a dense deformation field for 3-D robust registration. *IEEE Trans. Med. Imaging.*, 20:388–402.

Hibbard, L., Arnicar-Sulze, T., Dovey-Hartman, B., and Page, R. 1992. Computed alignment of dissimilar images for three-dimensional reconstructions. *J. Neurosci. Methods.*, 41:133–152.

Hibbard, L., and Hawkins, R. 1988. Objective image alignment for three-dimensional reconstruction of digital autoradiograms. *J Neurosci. Meth.*, 26:55–74.

Hibbard, L., McGlone, J., Davis, D., and Hawkins, R. 1987. Three-dimensional representation and analysis of brain energy metabolism. *Science*, 236:1641–1646.

Hill, D., Batchelor, P., Holden, M., and Hawkes, D. 2001. Medical image registration. *Phys. Med. Biol.*, 46: R1–R45.

Hoehn, M., Küstermann, E., Blunck, J., Wiedermann, D., Trapp, T., Wecker, S., Föking, M., Arnold, H., Hescheler, J., Fleischmann, B., Schwindt, W., and Bührle, C. 2002. Monitoring of implanted stem cell migration in vivo: a highly resolved in vivo magnetic resonance imaging investigation of experimental strocke in rat. *Proc. Nat. Acad. Sci.*, 99:16267–16272.

Holden, M., Hill, D.H., Denton, E., Jarosz, J., Cox, T., Rohlfing, T., Goodey, J., and Hawkes, D. 2000. Voxel similarity measures for 3-D serial MR brain image registration. *IEEE Trans. Med. Imaging.*, 19:94–102.

Horn, B. and Schunck, B. 1981. Determining optical flow. *Art. Intell.*, 17:185–204.

Hsu, C., Wu, M., and Lee, C. 2001. Robust image registration for functional magnetic resonance imaging of the brain. *Med. Biol. Eng. Comput.*, 39:517–524.

Hu, M. 1962. Visual pattern recognition by moment invariants. *IEEE Trans. Inform. Theory.*, 8:179–187.

Iosifescu, D., Fitzpatrick, J., Wang, M., Galloway, R.J., Maciunas, R., Allen, G., Shenton, M., Warfield, S., Kikinis, R., Dengler, J., Jolesz, F., and McCarley, R. 1997. An automated registration algorithm for measuring MRI subcortical brain structures. *Neuroimage*, 6:13–25.

Jacobs, M., Windham, J., Soltanian-Zadeh, H., Peck, D., and Knight, R. 1999. Registration and warping of magnetic resonance images to histological sections. *Med. Phys.*, 26:1568–1578.

Jannin, P., Fleig, O., Seigneuret, E., Grova, C., Morandi, X., and Scarabin, J. 2000. A data fusion environment for multimodal and multi-informational neuronavigation. *Comput. Aided. Surg.*, 5:1–10.

Johnson, E. and Capowski, J. 1983. A system for the three-dimensional reconstruction of biological structures. *Comp. Biomed. Res.*, 16:79–87.

Johnson, H. and Christensen, G. 2001. Landmark and intensity-based, consistent thin-plate spline image registration. *LNCS*, 2082:329–343.

Joshi, S. and Miller, M. 2000. Landmark matching via large deformation diffeomorphisms. *IEEE Trans. Image. Proc.*, 9:1357–1370.

Juan, M., Alcaniz, B., Hernandez, V., Montesinos, A., Barcia, J., Monserrat, C., and Grau, V. 2000. A new efficient method for 3D registration using human brain atlases. *Stud. Health. Technol. Inform.*, 70:153–155.

Kent, J. and Tyler, D. 1988. Maximum likelihood estimation for the wrapped Cauchy distribution. *J. Appl. Stat.*, 15:247–254.

Kiebel, S., Ashburner, J., Poline, J., and Friston, K. 1997. MRI and PET coregistration–a cross validation of statistical parametric mapping and automated image registration. *Neuroimage*, 5:271–279.

Kosevich, A. 1995, *Theory of Elasticity*. 3rd Ed. Butterworth Heinemann, Oxford.

Kostelec, P., Weaver, J., and Healy, D. J. 1998. Multiresolution elastic image registration. *Med. Phys.*, 25:1593–1604.

Kremser, C., Plangger, C., Boesecke, R., Pallua, A., Aichner, F., and Felber, S. 1997. Image registration of MR and CT images using a frameless fiducial marker system. *Mag. Res. Imag.*, 15:579–585.

Kuglin, C. and Hines, D. 1975. The phase correlation image alignment method. *Proc. IEEE Int. Conf. Cyb. Soc.*, 163–165.

Kuljis, R. and Rakic, P. 1990. Hypercolumns in primate visual cortex can develop in the absence of cues from photoreceptors. *Proc. Natl. Acad. Sci. USA*, 87:5303–5306.

Kullback, S. and Leibler, R. 1951. On information and sufficiency. *Ann. Math. Statist.*, 122:79–86.

Lamadø , W., Glombitza, G., Demiris, A., Cardenas, C., Thorn, M., Meinzer, H., Grenacher, L., Bauer, H., Lehnert, T., and Herfarth, C. 2000. The impact of 3-dimensional reconstructions on operation planing in liver surgery. *Arch. Surg.*, 135:1256–1261.

Lester, H. and Arridge, S. 1999. A survey of hierarchical non-linear medical image registration. *Pat. Rec.*, 32:129–149.

Likar, B. and Pernus, F. 1999. Automatic extraction of corresponding points for the registration of medical images. *Med. Phys.*, 26:1678–1686.

Lurie, A. 1990, *Nonlinear Theory of Elasticity*. North-Holland: Amsterdam.

Macagno, E., Levinthal, C., and Sobel, I. 1979. Three-dimensional computer reconstruction of neurons and neuronal assemblies. *Annu. Rev. Biophys. Bioeng.*, 8:323–351.

Macagno, E., Levinthal, C., Tountas, C., Bornholdt, R., and Abba, R. 1976, *Recording and Analysis of 3-D Information from Serial Section Micrographs: The Cartos System*. Hemisphere Publishing Corporation: Washington, P.B. Brown: Computer technology in neuroscience edition.

MacDonald, D., Kabani, N., Avis, D., and Evans, A. 2000. Automated 3d extraction of inner and outer surfaces of cerebral cortex from MRI. *NeuroImage*, 12:340–356.

Maintz, J. and Viergever, M. 1981. A survey of medical image registration. *Med. Image. Anal.*, 2:1–36.

Malandain, G. and Bardinet, E. 2003. Intensity compensation within series of images. *LNCS*, 2879:41–49.

Malandain, G., Bardinet, E., Nelissen, K., and Vanduffel, W. 2004. Fusion of autoradiographs with an MR volume using 2-D and 3-D linear transformations. *NeuroImage*, 23:111–127.

Maurer, C. and Fitzpatrick, J. 1993. *Interactive Image-Guided Neurosurgery.* R.J. Maciunas (Ed.). *A review of medical image registration*, American Association of Neurological Surgeons, Park Ridge, IL, pp. 17–44.

Maurer, C., Fitzpatrick, J., Wang, M., Galloway, R., Maciunas, R., and GS, G.A. 1997. Registration of head volume images using implantable fiducial markers. *IEEE Trans. Med. Imag.*, 16:447–462.

Maurer, C., Hill, D., Martin, A., Liu, H., McCue, M., Rueckert, D., Lloret, D., Hall, W., Maxwell, R., Hawkes, D., and Truwit, C. 1998a. Investigation of intraoperative brain deformation using a 1.5-T interventional MR system: preliminary results. *J. Anat.*, 193:347–361.

Maurer, C., Hill, D., Martin, A., Liu, H., McCue, M., Rueckert, D., Lloret, D., Hall, W., Maxwell, R., Hawkes, D., and Truwit, C. 1998b. Investigation of intraoperative brain deformation using a 1.5-T interventional MR system: preliminary results. *IEEE Trans. Med. Imaging.*, 17:817–825.

Maurer, C., Maciunas, R., and Fitzpatrick, J. 1998c. Registration of head CT images to physical space using a weighted combination of points and surfaces. *IEEE Trans. Med. Imaging.*, 17:753–761.

McInerney, J. and Roberts, D. 1998. An object-based volumetric deformable atlas for the improved localization of neuroanatomy in MR images. *LNCS*, 1496:861–869.

Mega, M., Berdichevsky, D., Levin, Z., Morris, E., Fischman, A., Chen, S., Thompson, P., Woods, R., Karaca, T., Tiwari, A., Vinters, H., Small, G., and Toga, A. 1997. Mapping histology to metabolism: Coregistration of stained whole-brain sections to premortem PET in Alzheimer's disease. *Neuroimage*, 5:147–153.

Miller, K. and Chinzei, K. 1997. Constitutive modelling of brain tissue: experiment and theory. *J. Biomech.*, 30:1115–1121.

Modersitzki, J. 2004, *Numerical Methods for Image Registration*. Oxford University Press.

Modersitzki, J., Obelöer, W., Schmitt, O., and Lustig, G. 1999. Elastic matching of very large digital images on high performance clusters. *LNCS*, 1593:141–149.

Mountcastle, V. 1997. The columnar organization of the neocortex. *Brain*, 120:701–722.

Murphy, M., O'Brien, T., Morris, K., and Cook, M. 2001. Multimodality image-guided epilepsy surgery. *J. Clin. Neurosci.*, 8:534–538.

Mutic, S., Hellier, P., Barillot, C., Dempsey, J., Bosch, W., Low, D., Drzymala, R., Chao, K., Goddu, S., Cutler, P., and Purdy, J. 2001. Multimodality image registration quality assurance for conformal three-dimensional treatment planning. *Int. J. Radiat. Oncol. Biol. Phys.*, 51:255–260.

Nowinski, W., Scarth, G., Somorjai, R., Fang, A., Nguyen, B., Raphel, J., Jagannathan, L., Raghavan, R., Bryan, R., and Miller, G. 1997. Multiple brain atlas database and atlas-based neuroimaging system. *Comput. Aided. Surg.*, 2:42–66.

Nowinski, W. and Thirunavuukarasuu, A. 2001. Atlas-assisted localization analysis of functional images. *Med. Image. Anal.*, 5:207–220.

Okajima, K. 1986. A mathematical model of the primary cortex and hypercolumn. *Biol. Cyber.*, 54:107–114.

Ongaro, I., Sperber, G., Machin, G., and Murdoch, C. 1991. Fiducial points for three-dimensional computer-assisted reconstruction of

serial light microscopic sections of umbilical cord. *Anat. Rec.*, 229:285–289.

Otte, M. 2001. Elastic registration of fMRI data using Bezier-spline transformations. *IEEE Trans. Med. Imaging.*, 20:193–206.

Ourselin, S., Bardinet, E., Dormont, D., Malandain, G., Roche, A., Ayache, N., Tandé, D. Parain, K., and Yelnik, J. 2001a. Fusion of histological sections and MR images: towards the construction of an atlas of the human basal ganglia. *LNCS*, 2208:743–751.

Ourselin, S., Roche, A., Subsol, G., Pennec, X., and Ayache, N. 2001b. Reconstructing a 3D structure from serial histologic sections. *Image. Vis. Comp.*, 19:25–31.

Ozturk, C. 2002. Align1.1. http://www.neuroterrain.org/˜webby/production/body/index.html.

Palm, G. 1982, *Studies of Brain Function: Neural Assemblies*. Springer: Berlin.

Pawley, J. 1995, *Handbook of Biological Confocal Microscopy*. Plenum: New York.

Penney, G., Weese, J., Little, J., Desmedt, P., Hill, D., and Hawkes, D. 1998. A comparison of similarity measures for use in 2-D-3-D medical image registration. *IEEE Trans. Med. Imaging.*, 17:586–595.

Perkins, W. and Green, R. 1982. Three-dimensional reconstruction of biological sections. *J. Biomed. Eng.* 4:37–43.

Rangarajan, A., Chui, H., and Duncan, J. 1999. Rigid point feature registration using mutual information. *Med. Image. Anal.*, 3:425–440.

Rangarajan, A., Chui, H., Mjolsness, E., Pappu, S., Davachi, L., Goldman-Rakic, P., and Duncan, J. 1997. A robust point matching algorithm for autoradiographic alignment. *Med. Image. Anal.*, 4:379–398.

Rohlfing, T. and Maurer, C. 2001. Intensity-based non-rigid registration using adaptive multilevel free-form deformation with an incompressibility constraint. *LNCS*, 2208:111–119.

Rohlfing, T., West, J., Beier, J., Liebig, T., Taschner, C., and Thomale, U. 2000. Registration of functional and anatomical MRI: accuracy assessment and application in navigated neurosurgery. *Comput. Aided. Surg.*, 5:414–425.

Rohr, K., Stiehl, H., Sprengel, R., Buzug, T., Weese, J., and Kuhn, M. 2001. Landmark-based elastic registration using approximating thin-plate splines. *IEEE Trans. Med. Imaging.*, 20:526–534.

Rouet, J., Jacq, J., and Roux, C. 2000. Genetic algorithms for a robust 3-D MR-CT registration. *IEEE Trans. Inf. Technol. Biomed.*, 4:126–136.

Rueckert, D., Sonoda, L., Hayes, C., Hill, D., Leach, M., and Hawkes, D. 1999. Nonrigid registration using free-form deformations: application to breast MR images. *IEEE Trans. Med. Imaging.*, 18:712–721.

Rusinek, H., Tsui, W.-H., Levy, A., Noz, M., and de Leon, M. 1993. Principal axes and surface fitting methods for three-dimensional image registration. *J. Nuc. Med.*, 34:2019–2024.

Russo, R. 1996, *Mathematical Problems in Elasticity*. World Scientific Publ: Singapore.

Sabbah, P., Zagrodsky, V., Foehrenbach, H., Dutertre, G., Nioche, C., DeDreuille, O., Bellegou, N., Mangin, J., Leveque, C., Faillot, T., Gaillard, J., Desgeorges, M., and Cordoliani, Y. 2002. Multimodal anatomic, functional, and metabolic brain imaging for tumor resection. *Clin. Imaging.*, 26:6–12.

Santori, E. and Toga, A. 1993. Superpositioning of 3-dimensional neuroanatomic data sets. *J. Neurosci. Methods.*, 50:187–196.

Schieweck, F. 1993. A parallel multigrid algorithm for solving the Navier-Stockes equations. *Imp. Comp. Sci. Eng.*, 5:345–378.

Schlaug, G., Schleicher, A., and Zilles, K. 1995. Quantitative analysis of the columnar arrangement of neurons in the human cingulate cortex. *J. Comp. Neurol.*, 351:441–452.

Schmitt, O. and Eggers, R. 1997a. High contrast and homogeneous staining of paraffin sections of whole human brains for three dimensional ultrahigh resolution image analysis. *Biotech. Histochem.*, 73:44–51.

Schmitt, O. and Eggers, R. 1997b. Systematic investigations of the contrast results of histochemical stainings of neurons and glial cells in the human brain by means of image analysis. *Micron*, 28:197–215.

Schmitt, O. and Eggers, R. 1999. Flat-bed scanning as a tool for quantitative neuroimaging. *J. Microsc.*, 196:337–346.

Schmitt, O., Eggers, R., and Modersitzki, J. 2005. Videomicroscopy, image processing, and analysis of whole histologic sections of the human brain. *Micr. Res. Tech.*, 66:203–218.

Schmitt, O., Modersitzki, J., and Obelöer, W. 1999. The human neuroscanning project. *Neuroimage*, 9:S22.

Schmolke, C. 1996. Tissue compartments in laminae II-V of rabbit visual cortex–three-dimensional arrangement, size and developmental changes. *Anat. Embryol.*, 193:15–33.

Schmolke, C. and Fleischhauer, K. 1984. Morphological characteristics of neocortical laminae when studied in tangential semithin sections through the visual cortex of the rabbit. *Anat. Embryol.*, 169:125–133.

Schormann, T. 1996. A new approach to fast elastic alignment with applications to human brains. *LNCS*, 1131:337–342.

Schormann, T., Darbinghaus, A., and Zilles, K. 1997. Extension of the principle axes theory for the determination of affine transformations. *Informatik aktuell*, 19:384–391.

Schormann, T. and Zilles, K. 1997. Limitations of the principal axes theory. *IEEE Trans. Med. Imag.*, 16:942–947.

Schormann, T. and Zilles, K. 1998. Three-dimensional linear and nonlinear transformations: an integration of light microscopical and MRI data. *Hum. Brain. Mapp.*, 6:339–347.

Silva, A. and Koretsky, A. 2002. Laminar specificity of functional MRI onset times during somatosensory stimulation in rat. *Proc. Nat. Acad. Sci.*, 99:15182–15187.

Sjöstrand, R. 1958. Ultrastructure of retinal rod synapses of the guinea pig eye as revealed by 3-D reconstructions from serial sections. *J. Ultrastruct. Res.*, 2:122–170.

Sokolnikoff, I. 1956, *Mathematical Theory of Elasticity*. McGraw-Hill: New York.

Street, C. and Mize, R. 1983. A simple microcomputer-based three-dimensional serial reconstruction system (MICROS). *J. Neurosci. Meth.*, 7:359–375.

Studholme, C., Hill, D., and Hawkes, D. 1999. An overlap invariant entropy measure of 3D medical image alignment. *Pat. Recog.*, 32:71–86.

Symon, K. 1971, *Mechanics*. 3rd edition, Addison-Wesley: Reading, MA.

Tanaka, S. 1991. Theory of ocular dominance column formation. *Biol. Cyber.*, 64:263–272.

Thirion, J.-P. 1998. Image matching as a diffusion process: An analogy with Maxwell's demons. *Med. Image. Anal.*, 2:243–260.

Thompson, J., Peterson, M., and Freeman, R. 2003. Single-Neuron activity and tissue oxygenation in the cerebral cortex. *Science*, 299:1070–1072.

Thompson, M. and Ferziger, J. 1989. An adaptive multigrid technique for the incompressible Navier-Stockes equations. *J. Comp. Phys.*, 82:94–121.

Thurfjell, L., Bohm, C., and Bengtsson, E. 1995. CBA–an atlas-based software tool used to facilitate the interpretation of neuroimaging data. *Comput. Methods. Programs. Biomed.*, 47:51–71.

Toga, A. and Banerjee, P. 1993. Registration revisited. *J. Neurosci. Meth.*, 48:1–13.

Toga, A., Santori, E., Hazani, R., and Ambach, K. 1995. A 3D digital map of rat brain. *Brain. Res. Bull.*, 38:77–85.

Toga, A. and Thompson, P. 2001. The role of image registration in brain mapping. *Image. Vis. Comp.*, 19:3–24.

van den Elsen, P., Pol, E.-J., and Viergever, M. 1993. Medical image matching - a review with classification. *IEEE Eng. Med. Biol.*, 12:26–39.

van Essen, D. 1997. A tension-based theory of morphologenesis and compact wiring in the central nervous system. *Nature*, 285:313–318.

Vatsa, V. and Wedan, B. 1990. Development of a multigrid code for 3-D Navier-Stokes equations and its application to a grid-refinement study. *Comp. Fluids.*, 18:391–403.

Viergever, M., Maintz, J., and Stokking, R. 1997. Integration of functional and anatomical brain images. *Biophys. Chem.*, 68:207–219.

Viola, P. and Wells, W. 1993. Alignment by maximization of mutual information—a review with classification. *5th Int. Conf. Comp. Vis., IEEE*, 5:16–23.

Viola, P. and Wells, W.: 1997. Alignment by maximization of mutual information. *Int. J. Comp. Vision.*, 24:137–154.

Ware, R. and LoPresti, V. 1975. Three-Dimensional reconstruction from serial sections. *Int. Rev. Cytol.*, 40:325–440.

Watanabe, H., Andersen, F., Simonsen, C., Evans, S., Gjedde, A., and Cumming, P. 2001. MR-based statistical atlas of the Gottingen minipig brain. *Neuroimage*, 14:1089–1096.

Webster, R. 1994. An algebraic multigrid solver for Navier-Stokes problems. *Int. J. Num. Meth. Fluids.*, 18:761–780.

West, J., Fitzpatrick, J., Toms, S., Maurer, C., and Maciunas, R. 2001. Fiducial point placement and the accuracy of point-based, rigid body registration. *Neurosurgery*, 48:810–817.

White, E. 1989, *Cortical Circuits. Synaptic Organization of the Cerebral Cortex. Structure, Function, and Theory*. Birkhäuser, Boston.

Widrow, B. 1973. The rubber-mask technique. I. Pattern Measurement and analysis. *Pat. Recog.*, 5:175–197.

Woods, R. 2002. AIR 5.08. http://bishopw.loni.ucla.edu/AIR5/index.html.

Woods, R., Dapretto, M., Sicotte, N., Toga, A., and Mazziotta, J. 1999. Creation and use of a Talairach-compatible atlas for accurate, automated, nonlinear intersubject registration, and analysis of functional imaging data. *Hum. Brain. Mapp.*, 8:73–79.

Woods, R., Grafton, S., Holmes, C., Cherry, S., and Mazziotta, J. 1998a. Automated image registration: I. General methods and intrasubject, intramodality validation. *J. Comput. Assist. Tomogr.*, 22:139–152.

Woods, R., Grafton, S., Watson, J., Sicotte, N., and Mazziotta, J. 1998b. Automated image registration: II. Intersubject validation of linear and nonlinear models. *J. Comput. Assist. Tomogr.*, 22:153–165.

Yeshurun, Y. and Schwartz, E. 1999. Cortical hypercolumn size determines stereo fusion limits. *Biol. Cyber.*, 80:117–129.

You, J. 1995. Efficient image matching: A hierarchical chamfer matching scheme via distributed system. *Real-time Imag.*, 1:245–259.

Young, M. 1992. Objective analysis of the topological organization of the primate cortical visual system. *Nature*, 358:152–155.

Young, M. 1996, *The Analysis of Cortical Connectivity*. Springer.

Zeiss: 1992. *KS400 Reference Guide*. Zeiss Vision: Jena.

Zhao, W., Young, T., and Ginsberg, M. 1993. Registration and three-dimensional reconstruction of autoradiographic images by the disparity analysis method. *IEEE Trans. Med. Imag.*, 12:782–791.

Zhu, Y. 2002. Volume image registration by cross-entropy optimization. *IEEE Trans. Med. Imaging.*, 21:174–180.